Epsilon Metal Summary Report Fiscal Year 2011

Fuel Cycle Research & Development

Prepared for
U.S. Department of Energy
Separations and Waste Forms Campaign

D.M. Strachan, J.V. Crum, M.R. Zumhoff, C.C. Bovaird, C.F. Windisch, Jr. and B.J. Riley

Pacific Northwest National Laboratory

September 30, 2011

FCRD-WAST-2011-000389
PNNL-20975

SUMMARY

The Epsilon-metal (ε-metal) phase was selected in fiscal year (FY) 2009 as a potential waste form to immobilize the noble metals found in the undissolved solids, the soluble Tc, and the soluble noble metals, each resulting from proposed aqueous reprocessing. The ε-metal phase is observed in used nuclear fuel and in the uranium-bearing minerals in the natural reactors in Gabon, Africa, where the long-term corrosion behavior was demonstrated. This makes ε-metal a very attractive waste form.

Last fiscal year, ε-metal was successfully fabricated by combining the five metals—Mo, Ru, Rh, Pd and Re (surrogate for Tc)—into pellets followed by consolidation with an arc melter. The arc melter produced fully dense samples with the epsilon structure. However, some chemistry differences were observed. The microstructure that resulted from arc melting had regions rich in Re and Mo, and others rich in Pd, while Ru and Rh were fairly uniform.

This year, thermal stability (in air), corrosion testing of the samples fabricated by arc melting, and the initial evaluation of commercial methods for ε-metal consolidation were the main focus for experimental work. Three commercial methods were selected for evaluation based on a study of potential processing methods, published earlier this year.

Thermal stability was measured with a differential scanning calorimeter-thermogravimetric analyzer by heating the test specimens at a constant rate as well as heating step-wise, holding at each temperature for a defined time. There is clear evidence during ramp heating of an exothermic event with a simultaneous mass loss beginning at ~700 °C. Step heating showed that oxidation began at ~680 °C with minimal mass gain this is followed by mass loss at ~700 °C. We conclude that the ε-metal begins to oxidize at temperatures less than 680 °C; the higher oxidation state oxides of Mo and Re (Tc) are very volatile. These findings are useful for considering the effects of Voloxidation process on the undissolved solids composition.

Three pellet specimens of ε-metal were subjected to electrochemical testing to study the corrosion behavior under acidic, alkaline, saline, and "inert" conditions. Tests were conducted according to an interim procedure developed for the alloy metal waste forms. First, an open circuit potential was measured, followed by linear polarization sweeps. The Tafel equation was fit to the linear polarization sweep data to determine the corrosion rate of each pellet in each test solution. The average calculated corrosion rates of the three pellets according to solution conditions were as follows: 0.2(0.1)[a] μm/y (1 mM NaOH), 0.9(0.5) μm/y (0.01 M NaCl), 0.6(0.3) μm/y (1 mM H_2SO_4), 0.8(0.4) μm/y (1 mM NaOH + 0.01 M NaCl), 0.9(0.7) μm/y (1 mM H_2SO_4 + 0.01 M NaCl), and 1.5(0.7) μm/y (2 mM $Na_2B_4O_7 \cdot 10H_2O$ + 2 mM H_3BO_3). The overall average corrosion rate obtained for all pellets and in all solutions was 0.8(0.4) μm/y, which equates to 3×10^{-5} g/(m^2·d) in units commonly reported for most dissolution testing.

Three single-pass flow-through (SPFT) tests were conducted at a flow rate of 10 mL/day at 90 °C and pH of 2.5, 7.0, and 9.0 for up to 322 days. Test results indicate that the average dissolution rates were 2.8×10^{-4} g/(m^2·d) for Mo and Re irrespective of pH at 90 °C. The sample used for the pH 7.0 SPFT test contained extra Re compared to samples used for the other two SPFT tests, which came from a single pellet. These dissolution rates, albeit preliminary, are about 1,000 times less than typical dissolution rates for borosilicate glasses and about 10 times greater than those obtained from electrochemical tests. These data indicate the ε-metal phase is chemically durable.

[a] The number in () is the 1-sigma uncertainty in the last reported digit, i.e. in this case 0.2 ± 0.1 μm/y.

The arc melted specimens show there are two phases with the same structure P63/mm (hexagonal) and nearly identical unit cell dimensions. One of the phases is rich in Pd and the other in Mo and Re. These two phases appear to behave differently during dissolution in electrochemical and SPFT tests. Characterization of test specimens after testing indicates the dissolution is complex and involves oxidative dissolution followed by precipitation of both oxide and metallic phases. These data suggest the dissolution process is complex, involving the preferential dissolution of the Mo-Re-rich phase over the Pd-rich phase. However, this is further complicated by the precipitation of both metallic and oxide phases. More dissolution and electrochemical test are planned in an effort to determine the dissolution mechanism(s).

Commercial processes for the consolidation of the ε-metal phase were ranked and hot isostatic pressing, microwave sintering, and spark plasma sintering were selected for evaluation. Vendors for two of these— microwave sintering and spark plasma sintering—were identified this fiscal year and samples were shipped to both vendors for their initial tests. Only the samples that had been treated with microwave sintering were returned at the time this report was written. Characterization of these specimens showed that at 1550 °C, the original five metals (Mo, Pd, Re, Rh, and Ru) had reacted sufficiently to be nearly 100% converted to ε-metal. However, the sintered densities were about 50% of the theoretical density. A vendor for hot isostatic pressing had not been identified.

CONTENTS

FIGURES

TABLES

ACRONYMS

a	year(s)
BSE	backscattered electron
DSC	differential scanning calorimetry
EDS	energy dispersive spectroscopy
EW	equivalent weight
FY	fiscal year
Ga	giga-years (1 million years)
ICP-MS	inductively coupled plasma-mass spectroscopy
kV	kilovolt
Ma	mega-years (10^6 a)
mmol	millimoles (chemical quantity)
mM	millimolar (chemical concentration)
MS	mass spectrometry
mV	millivolt
MW	molecular weight
OM	optical microscopy
OPC	open circuit potential
PFA	perfluoroalkoxide (Teflon®)
SEI	secondary electron imaging
SEM	scanning electron microscopy
SPFT	single-pass flow through
SRNL	Savannah River National Laboratory
TGA	thermogravimetric analysis
THAM	tris hydroxymethyl aminomethane
XRD	X-ray diffraction

SEPARATIONS AND WASTE FORMS / ALTERNATIVE WASTE FORMS

1. INTRODUCTION

Some fission products formed during the irradiation of UO_2 are not very soluble in the UO_2 matrix. These elements can segregate from the matrix for form unique compounds. One such compound is ε-metal. This metal alloy appears as separate ~10-μm particles at the UO_2 grain boundaries and is composed of the elements Mo, Pd, Ru, Rh, and Tc (Cui et al. 2004; Kleykamp 1985, 1988, 1989; Kleykamp 2005; Kleykamp et al. 1985). These metal particles compose a large fraction of the residue in the fuel dissolvers used in reprocessing of irradiated UO_2 nuclear fuel. These same ε-metal particles or evidence of their presence were found in the natural reactors that were discovered in Gabon, Africa (Gauthier-Lafaye et al. 1996) and later characterized (Utsunomiya and Ewing 2006). Utsunomiya and Ewing present evidence that indicated the main isotope of concern, ^{99}Tc, only migrated a few centimeters over about 2 Ga, including the 0.5 Ma over which the reactors were active. The fact that the ε-metal does not dissolve in the strong HNO_3 used in the dissolvers and did not dissolve over 2 Ga suggests that it is an ideal waste form for ^{99}Tc ($t_{1/2}$ = 2.13 x 10^6 a) and ^{107}Pd ($t_{1/2}$ = 6.5 x 10^6 a). The work described here is in support of the development of the ε-metal phase as a waste form for Tc, Mo, and the noble metals (Ru, Rh, and Pd) separated during used nuclear fuel reprocessing.

Although the dissolution of the ε-metal phase would appear to be adequate for disposal purposes, a method is needed to convert the various streams containing noble metals and Tc into an alloy and consolidate the metal particles into a monolith with less surface area than the powder form that comes from the dissolution of irradiated UO_2. Because the repository geologies in the US are likely to be substantially different than the geology at the natural reactors in Gabon, dissolution and corrosion testing is needed.

Here we present the results from dissolution tests on consolidated ε-metal in which we substituted Re for Tc so that non-radioactive facilities could be used. Dissolution or corrosion tests were carried out with the single-pass flow-through (SPFT) test and an electrochemical test.

Additional methods of consolidating ε-metal and the Mo, Tc, and noble metals that are removed from the aqueous stream have been discussed by Rohatgi and Strachan (2011). Three of the recommended processes were selected. Sample pellets containing the five constituent metals were sent to vendors for microwave sintering and spark-source sintering; a vendor for hot-isostatic pressing has yet to be identified.

Initial results from the Voloxidation test (Goode and Stacy 1978; Jubin et al. 2009b; Jubin et al. 2009a) suggested that the ε-metal phase reacted with oxygen at elevated temperatures. Therefore, we briefly investigated the thermal stability of ε-metal in air. It had been shown to be stable up to ~1200 °C under vacuum (Strachan et al. 2010).

2. EXPERIMENTAL

The ε-metal development work in FY 2011 focused on the oxidative corrosion behavior testing and identifying additional processing techniques to produce the waste form. The following sections describe the experiments for electrochemical testing, SPFT, scanning electron microscopy (SEM), energy dispersive spectroscopy (EDS), optical microscopy (OM), and X-ray diffraction (XRD).

2.1 Sample Preparation

The samples used for testing were fabricated in FY 2010 by the arc melting, with the target compositions given in Table 1. The samples were batched from the five individual metals, pressed into pellets with a small amount of polyvinyl alcohol as a pressing aid, and further consolidated in a cold isostatic press at 6 GPa. The polyvinyl alcohol was removed by controlled heating to 600 °C. The resulting pellets were then arc melted. Further details are found in Strachan et al (2010).

Table 1. Target compositions of ε-metal coupons used in the tests described in this document.

Samples (pellets)	Mass Fraction				
	Mo	Pd	Re	Rh	Ru
Baseline (5-1, 5-2, 8, 9, 10)	0.373	0.116	0.175	0.028	0.308
Baseline +25%-Re	0.320	0.102	0.250	0.028	0.300

2.2 Differential Scanning Calorimeter / Thermogravimetric Analysis

A sample of the ε-metal was placed into a simultaneous differential scanning calorimeter – thermal gravimetric analysis (DSC-TGA; model Q600, TA Instruments, New Castle, DE) and either ramp heated at 5 °C/min in air up to 995 °C, or step heated starting at 680 °C in 10 °C steps, with a 10 min hold at each temperature up to 810 °C. The TGA signal was calibrated; however, it was not possible to accurately calibrate the DSC signal. Hence, the DSC data are qualitative.

2.3 Electrochemical Testing

Electrochemical testing was conducted following a protocol provided by Savannah River National Laboratory (SRNL) that was designed for testing the simulated alloy metal waste form (Appendix A). The electrochemical test cell (Figure 1) consisted of a corrosion kit (part# EL-CORR-1) and sample holder (part# EL-C-013) from BioLogic Science Instruments (Claix, France). The reference electrode was calomel (Hg_2Cl_2) and the counter electrodes were graphite. The cell was controlled with a Solartron 1470E Cell Test System (Solartron Analytical, Oak Ridge, TN) with Solartron MultiStat® and CorrView software packages for controlling the cell test system and for data analysis.

Figure 1. The electrochemical test cell used in testing the ε-metal samples.

Three specimens of ε-metal were cut into cylinders with electric discharge machining and thinned with a diamond wafer blade saw to fit into the sample holder. The testing surface was polished to a 600-grit finish, washed with deionized water, washed with ethanol, and then dried in nitrogen gas.

The specimen holder limits the exposed surface area to 0.785 cm^2. The samples were submerged in the test solution and aligned perpendicular to the graphite counter electrodes. Next, the calomel reference electrode was aligned such that the tip pointed to the center of the test specimen. Before the start of each test, nitrogen gas was bubbled through the solution for 30 minutes. The purge tube was raised above the solution to purge the head space of the test cell for the duration of the test.

The first segment of the test was a 4-h open circuit measurement with a data collection speed of 0.2 points/s to establish the open circuit potential (OCP). The second and third segments were identical linear polarization measurements starting at -0.03 V < OCP up to +0.03 V> OCP followed by a reverse scan. The forth segment was a linear polarization measurement starting at -0.03 V < OCP up to +1 V> OCP followed by a reverse scan. Near the end of FY 2011, it was determined that -0.03 V < OCP was insufficient to for fitting the cathodic side of the Tafel fit. Thus, the scan range was changed to -0.3 V < OCP up to +0.5 V> OCP. However, due to the limited time, the new scan range was only evaluated for inert solution. For segments 2, 3, and 4 measurements were done at a scan rate of 0.1 mV/s and data collection rate of 1 mV/point. Although these measurements were made, only the segment 4 data are reported here. This was the consensus of those working on the alloy waste form.

Test were conducted in the following solutions: basic (0. 1 mmol/kg NaOH), acidic (0. 1 mmol/kg H_2SO_4), brine (0.01 mol/kg NaCl), acidic + brine, basic + brine, and inert (2 mmol/kg $Na_2B_4O_7{\cdot}10H_2O$ + 2 mmol/kg H_3BO_3).

Corrosion rates were calculated by first performing automatic Tafel fits to the data with CorrView™ software to the selected data [Equation (1)]:

$$I = I_o \times \left(10^{(E-E_o)/\beta_a} + 10^{-(E-E_o)/\beta_c}\right) \quad (1)$$

The Tafel fit determines β_a, β, I_o, and E_o, where β= anodic Tafel slope, β_c = cathodic Tafel slope, I_o / E_o = current / voltage where anodic and cathodic lines intersect. Equation (2) was then used to calculate the corrosion rate in terms of µm/a.

$$\text{Corrosion rate } (\mu m/yr) = \frac{I_{corr} \times EW \times 10{,}000}{\rho \times 96500} \times 3.154 \times 10^7 \quad (2)$$

Where $I_{corr} = I_o$ (A/cm^2), determined in Equation (1), EW = 18.04 g/mol, ρ = 12.12 g/cm^3, 10,000 µm/cm conversion factor, 96 500 coulombs/mol, and 3.154×10^7 s/a conversion factor.

A 'manual' Tafel fit was performed by fitting only the anodic portion, relative to OCP, of the data. Additionally, the polarization resistance data (potential - vs. - current near the OCP) were fit to the Stern-Geary equation [Equation (3)] because unlike the Tafel equation it only requires a narrow range near the OCP to properly fit. While a full Tafel fit was preferred, most the data collected during FY 2011 may be more appropriately fit to the Stern-Geary Equation [Equation 3] or with the anodic only Tafel fits.

$$I_{corr} = \frac{\beta_a \beta_c}{2.3 R_p (\beta_a + \beta_c)} \quad (3)$$

Parameters for these fits were determined. The mole-fraction averaged atomic weight was calculated from the mole fractions of the elements reported in Table 1 and the atomic weight of the element. This yielded an average atomic weight of 108.26 g/mol. To calculate the number of electrons transferred in the reaction, the average change in oxidation state was used. Thus, Mo oxidizes to Mo^{6+} or 6 electrons; Pd, 2 electrons; Re, 7 electrons; Rh, 3 electrons; and Ru, 3 electrons. The mole-fraction, weighted average was 6 electrons. An equivalent weight of 18.04 equivalents/mol was obtained by dividing the average molecular weight by the number of electrons transferred. We recognize that only Mo and Re are likely to oxidize and go into solution, however, the area and the phase that is affected is, at this date,

unknown. Therefore, we assume that the corrosion is uniform and involves all elements equally, until we have sufficient information to make a better assignment. A density of 12.12×10^3 kg/m^3, measured with Archimedes method, was used for all calculations. These values were used in the Stern-Geary equation [Equation (3)] to obtain the corrosion current and, hence, the corrosion rate.

With respect to the number of electrons transferred, the value calculated here is a preliminary value. Once the corrosion reaction is fully understood, the correct number of electrons can be used, but until then, the value of 6 will be used.

2.4 Single-Pass Flow-Through Testing

Evaluation of dissolution of the ε-metal phase was performed using the SPFT test method. The SPFT apparatus provides for experimental flexibility allowing each of the kinetic test parameters to be isolated and quantified (McGrail 1997; McGrail and Peeler 1995; ASTM 2010). With the SPFT method, the temperature, flow rate, solution composition, and sample mass and size can all be manipulated to assure accurate rate determinations (Icenhower and Dove 2000; Icenhower et al. 2002; Icenhower et al. 2000; Icenhower et al. 2003; Pierce et al. 2005; Wellman et al. 2006; Wellman et al. 2005; ASTM 2010).

In general, the SPFT system (Figure 2) consists of a programmable pump that transports solutions from an influent reservoir through Teflon® tubing.

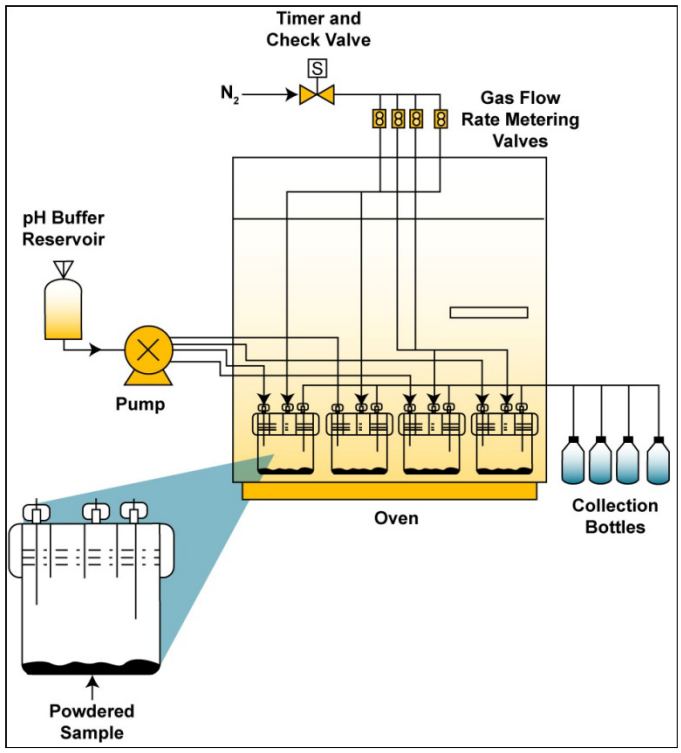

Figure 2. Schematic of the single-pass flow-through dissolution test system**.** (Note: figure shows powder samples, however, monoliths were used.)

Solution is transferred into 40-mL capacity perfluoroalkoxide (PFA) reactors (Savillex, Minnetonka, MN). The reactors are situated within constant temperature ovens, whose temperature is controlled to ±2 °C with calibrated thermocouples. The metal coupon rested on a raised PFA mesh basket that ensures solution contact on all sides of the coupon. Influent and effluent solutions enter and exit, respectively, from fluid transfer lines that protrude through two separate ports in the vessel top. The residence time of

the solution in the reactor varies with the flow rate, which is adjusted in accordance to the needs of the experiment. The effluent line carries solution to collection vials that are positioned outside the oven.

In general, this test can be performed under any redox condition. In the current study, ambient oxygen fugacity was used, i.e. no control of redox. Effluent solution was collected continuously and aliquots of the effluent were retained for pH measurement and analysis with inductively coupled plasma-mass spectroscopy (ICP-MS). Solutions earmarked for analysis with ICP-MS were preserved by making the solution acidic with Optima™ HNO_3 (Fisher Scientific, Pittsburgh, PA). Concentrations of Mo, Pd, Re, Rh, and Ru in the leachates were used to quantify the dissolution rates of the coupons. Before the sample specimens were added to the reactor, blank solution samples were collected and used to establish the concentration of background analytes. The blank samples were treated in exactly the same manner as the samples.

To obtain accurate dissolution rates, the test must be run sufficiently long that steady state is achieved. This is usually done by allowing the test to run until several solution analyses show that the rate has remained unchanged within experimental uncertainty.

2.4.1 Rate Calculations and Uncertainty

Dissolution rates, based on steady-state concentrations of elements in the effluent solution, are normalized to the amount of the element present in the sample by the following formula shown in Equation (4):

$$r_i = \frac{\left(C_i - \overline{C}_{i,b}\right) q}{f_i S} \tag{4}$$

Where:

r_i = normalized dissolution rate for element i (g m^{-2} d^{-1})
C_i = concentration of the element i in the effluent (g L^{-1})
$\overline{C}_{i,b}$ = average background concentration of the element of interest (g L^{-1})
q = flow rate (L d^{-1})
f_i = mass fraction of the element in the metal (dimensionless)
S = surface area of the sample (m^2).

Optical micrographs of the test samples were captured with an Olympus SZH10 (Olympus, Center Valley, Pennsylvania) and with these micrographs, the surface areas were measured with Adobe Photoshop CS5 Extended Edition software. The surface sample was manually selected using the quick selection software tool to measure the area in pixels. A calibration micrograph of a ruler was used to make the conversion from pixels to meters (Table 2).

Table 2. Calculated surface area of metal coupons.

Metal coupon	Surface Area, m^2
Pellet 5-1	6.96×10^{-4}
Pellet 5-2	5.88×10^{-4}
Pellet 25%-Re	1.84×10^{-4}

The value of f_i was calculated from the chemical composition of the sample (Table 1). Flow rates were determined by gravimetric analysis of the fluid collected in each effluent collection vessel upon sampling. The background concentration of the element of interest is determined, as discussed previously, by analyses of the starting input solution and three blank solutions. Typically, background concentrations of elements are below their respective detection threshold. The detection threshold of any element is defined as the lowest calibration standard that can be determined reproducibly during an analytical run within 10%. In cases where the analyte is below the detection threshold, the background concentration of the element is set at the value of the detection threshold.

Determining the experimental uncertainty of the dissolution rate addresses uncertainties of each parameter in Equation (4). For uncorrelated random errors, the standard deviation of a function $f(x_1, x_2,\ldots x_n)$ is given by the delta method in Equation (5):

$$\sigma_f = \sqrt{\sum_{i=1}^{n}\left(\frac{\partial f}{\partial x_i}\right)^2 \sigma_i^2} \tag{5}$$

where

σ_f = standard deviation of the function f
x_i = parameter i
σ_I = standard deviation of parameter i.

Substituting Equation (4) into (5) results in the following Equation (6):

$$\sigma_{r_i} = \sqrt{\left(\frac{q}{f_i S}\right)^2 (\sigma_{C_i}^2 + \sigma_{\bar{C}_{i,b}}^2) + \left(\frac{C_i - \bar{C}_{i,b}}{f_i S}\right)^2 \sigma_q^2 + \left(\frac{(C_i - \bar{C}_{i,b})q}{f_i^2 S}\right)^2 \sigma_{f_i}^2 + \left(\frac{(C_i - \bar{C}_{i,b})q}{f_i S^2}\right)^2 \sigma_S^2} \tag{6}$$

Equation (5) can also be expressed in terms of the relative error, $\hat{\sigma}_{r_i} = \sigma_{r_i} / r_i$, and is given by Equation (7):

$$\hat{\sigma}_{r_i} = \sqrt{\frac{\left(\hat{\sigma}_{C_i} C_i\right)^2 + \left(\hat{\sigma}_{\bar{C}_{i,b}} \bar{C}_{i,b}\right)^2}{\left(C_i - \bar{C}_{i,b}\right)^2} + \hat{\sigma}_q^2 + \hat{\sigma}_{f_i}^2 + \hat{\sigma}_S^2} \tag{7}$$

Relative errors of 10%, 10%, 5%, 3%, and 15% for C_i, $\bar{C}_{i,b}$, q, f_i, and S, respectively, are typical for measurements conducted at Pacific Northwest National Laboratory. However, to reduce the error associated with mass fraction (f_i), the samples used in these experiments were ground, homogenized, sub-sampled, and analyzed at least three times to obtain a more accurate composition with a better estimate of the uncertainty. The conservative appraisal of errors assigned to the parameters in Equation (7), in addition to the practice of imputing detection threshold values to background concentrations, results in typical uncertainties of approximately ±35% RSD on the dissolution rate.

2.4.2 Buffer Solutions

The pH values of the solutions used in these experiments spanned the range from 2.5 to 9. The solutions used to control the pH during the SPFT experiments are summarized in Table 3, which also contains a summary of the in situ pH values computed at each test temperature with EQ3NR (Wolery 1992). It is important to address the change in pH that occurs at different temperatures when computing dissolution rates from SPFT data because the in situ pH can vary by as much as 1.5 pH units over the temperature range from 23 to 90 ºC. The buffer solutions for the pellet 5-2 and the pellet 25%-Re experiments were prepared by adding tris hydroxymethyl aminomethane (THAM) to 18 MΩ deionized water and adjusting the solution to the desired pH with concentrated nitric acid. For the pellet 5-1 test, concentrated nitric acid was added to deionized water. The pH of effluent solutions from each test was measured to check that the solution pH did not deviate during the experiment.

Table 3. Composition of solutions used in SPFT experiments. Solution pH values above 23 °C were calculated using the EQ3NR Code V7.2b database

Solution	Composition	pH @ T (°C)			
		23	40	70	90
Pellet 5-1	0.0035 M HNO_3	2.48	2.48	2.47	2.47
Pellet 5-2	0.05 M THAM + 0.0041 M HNO_3	8.99	8.67	8.08	7.72
Pellet 25%-Re	0.05 M THAM + 0.047 M HNO_3	7.01	6.57	5.91	5.55

2.5 Scanning Electron Microscopy / Energy Dispersive Spectroscopy

Following electrochemical and SPFT corrosion tests, samples were examined in a JEOL 5900 SEM (JEOL U.S.A., Peabody, MA) equipped with an EDAX silicon-drifted EDS detector (AMETEK, Mahwah, NJ), to characterize the corrosion process and products. The accelerating voltage of the electron beam was set to 6 kV to minimize beam penetration to an estimated depth of 155 nm with the Kanaya-Okayama Range equation [Equation (8)]:

$$R_{KO} = 0.0276 \times A \times E_0^{1.67} / Z^{0.89} \times \rho \qquad (8)$$

Where E_0 is the accelerating voltage (V) and the average of mixture of elements was taken for A = atomic weight (g/mol), Z, and density (g/cm^3).

Micrographs were collected with either a secondary electron (SEI) and/or backscattered electron (BSE) detectors. Elemental spot analysis was collected on surface features (altered surfaces). Elemental dot maps were collected to show the distribution of Mo, Re, Ru, Rh, Pd, and O at the exposed surface.

2.6 Optical Microscopy

Reflected light optical micrographs (color) of the altered surface of specimens after electrochemical testing were collected with an Olympus PMG3 inverted light microscope equipped with a single polarizer. Images were taken at 100×, 200×, 500×, and 1000× with polarized reflected light. The scale bar was calibrated with images of a ruler (with 10 µm steps), supplied with the microscope.

2.7 X-ray Diffraction

Samples of as-fabricated ε-metal were placed in liquid nitrogen rapidly followed by crushing in a hardened steel fixture. This allowed researchers to generate small ε-metal particles. This step was done because it was almost impossible to file or grind the bulk ε-metal. The particles were placed onto a zero-background silicon holder. Samples that were subjected to either electrochemical or SPFT testing were mounted as a monolith in a plastic holder. These samples were then loaded into a Bruker D8 Advance Diffractometer (Bruker AXS, Inc., Madison, WI). This XRD is configured with a Cu Kα X-ray target (λ = 15.406 nm), goniometer radius of 250 mm, 0.3° fixed divergence slit, and LynxEye™ position sensitive detector with an angular range of 3° 2θ. Samples were scanned from 10°–90° 2θ at a step size of 0.015° 2θ with a hold time between 0.3 and 1.5 s/step.

Phases were identified with Jade 6.0 software (Materials Data Inc., Livermore, CA) and both the International Center of Crystallographic Data PDF2 release 1999 and the International Center of Structure Data release 2004. Whole pattern fitting was done with Bruker TOPAS 4.2 software to determine fractions of the crystalline phases.

3. RESULTS AND DISCUSSION

3.1 Thermal Stability

Thermal stability of ε-metal (pellet 8) was examined with DSC-TGA both by heating at 5 °C/min to 995 °C (Figure 3), and then by step-heating from 680 °C to 810 °C making 10 °C steps, with a 10 min hold at each step (Figure 4). The ε-metal appeared thermally stable in air up to about 700 °C, at a ramp rate of 5 °C/min, the beginning of an exothermic peak (denoted as first downward peak in Figure 3) that coincides with the beginning of a mass loss at about 700 °C. However, when step-heated (Figure 4), ε-metal shows a mass gain starting at 680 °C (the first step/hold *T* used), which is a good indication that oxidation began at or below 680 °C, followed by mass loss beginning at 700 °C and continuing through 810 °C (maximum *T* for test). Both the ramp heating and step-heating show two mass loss rates. Step-heating experiment was necessary because the ramp heating rate was faster than the mass gain from oxidation. Mass loss on oxidation was expected, since Re and Mo form volatile oxides. The step heating experiment shows the mass gain, concluded to be oxidation, followed by mass losses at several different rates.

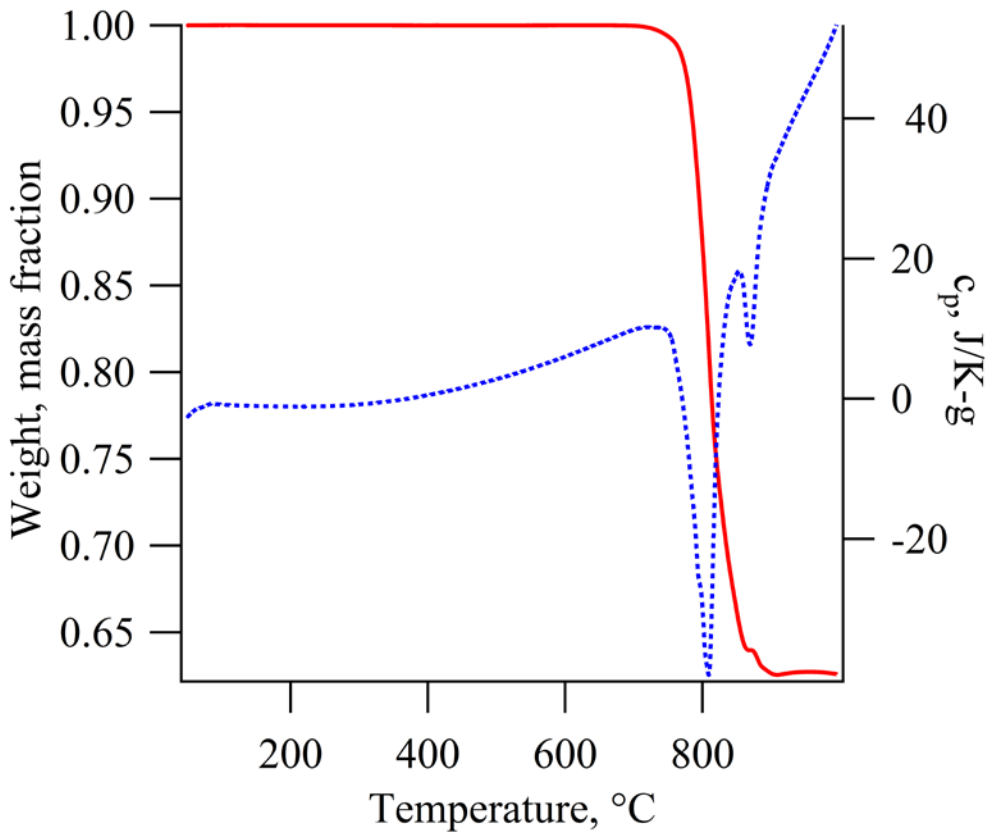

Figure 3. Mass loss (red) and specific heat capacity (blue dashed) of ε–metal (pellet 8) with temperature in air at a heating rate of 5 °C/min.

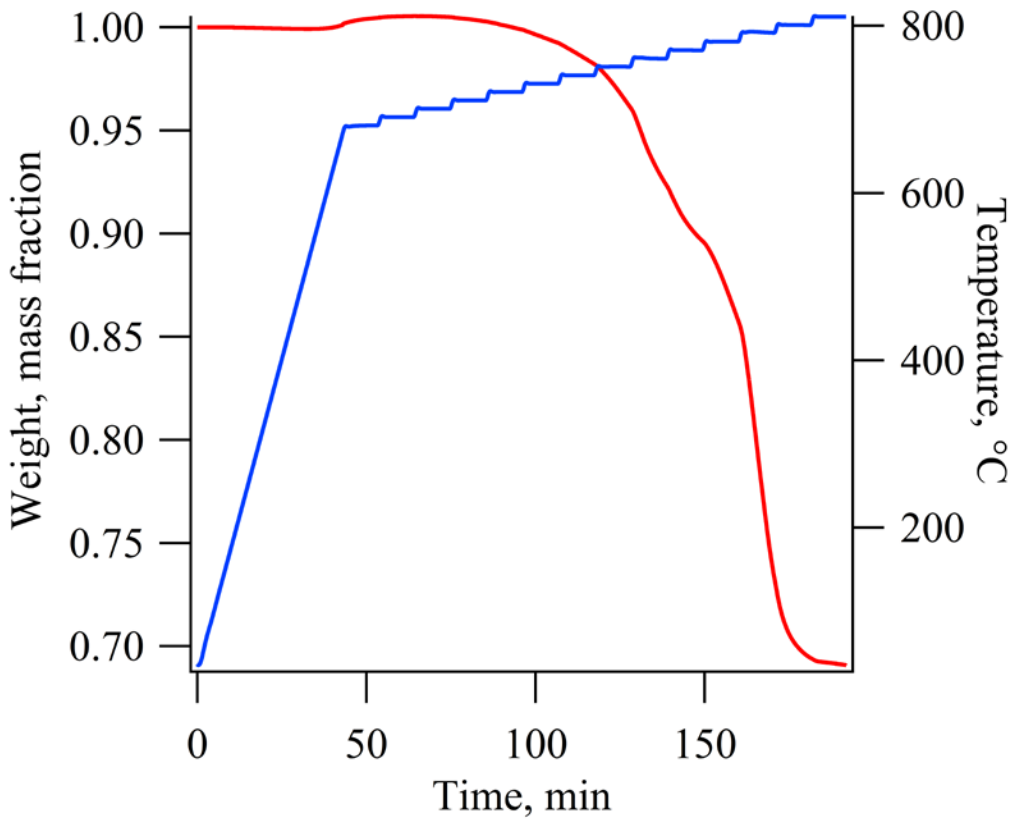

Figure 4. Mass loss (red) of ε–metal (pellet 8) with temperature (blue) and time by step heating (10 °C steps and 10 min holds).

After the ramp heating DSC-TGA experiment, pellet 8 was analyzed with SEM-EDS and XRD to characterize the changes in chemistry and crystal structure. Backscattered electron micrographs of pellet 8 (Figure 5) show a highly porous surface covered with small bright spheres and grey fibrous material. There is also a relief pattern shown (Figure 5) that is possible evidence of two chemically different, but structurally identical phases, preferentially oxidized and volatilized. Figure 6 shows the elemental dot map collected with SEM-EDS along one of the cracks seen in Figure 5a and 5b, showing the distribution of O, Al, Pd, Ru, Rh, Re, and Mo. The Al is suspected to be from the alumina crucible used to hold the sample in the DSC-TGA experiment. Comparing the O map with the Pd, Ru, Rh, Re, and Mo maps shows that portions of Pd, Re, and Mo have formed metal beads concentrated along the crack in the sample surface. However, most of the sample surface appears to be oxidized, especially Ru, Rh, and Re and to a lesser extent Pd and Mo. The reason Mo, Re, and Pd metal beads formed is unknown. However it is possible that as Mo, Re, and Pd oxidize they become volatile and partially re-condense as metals on the outer surfaces.

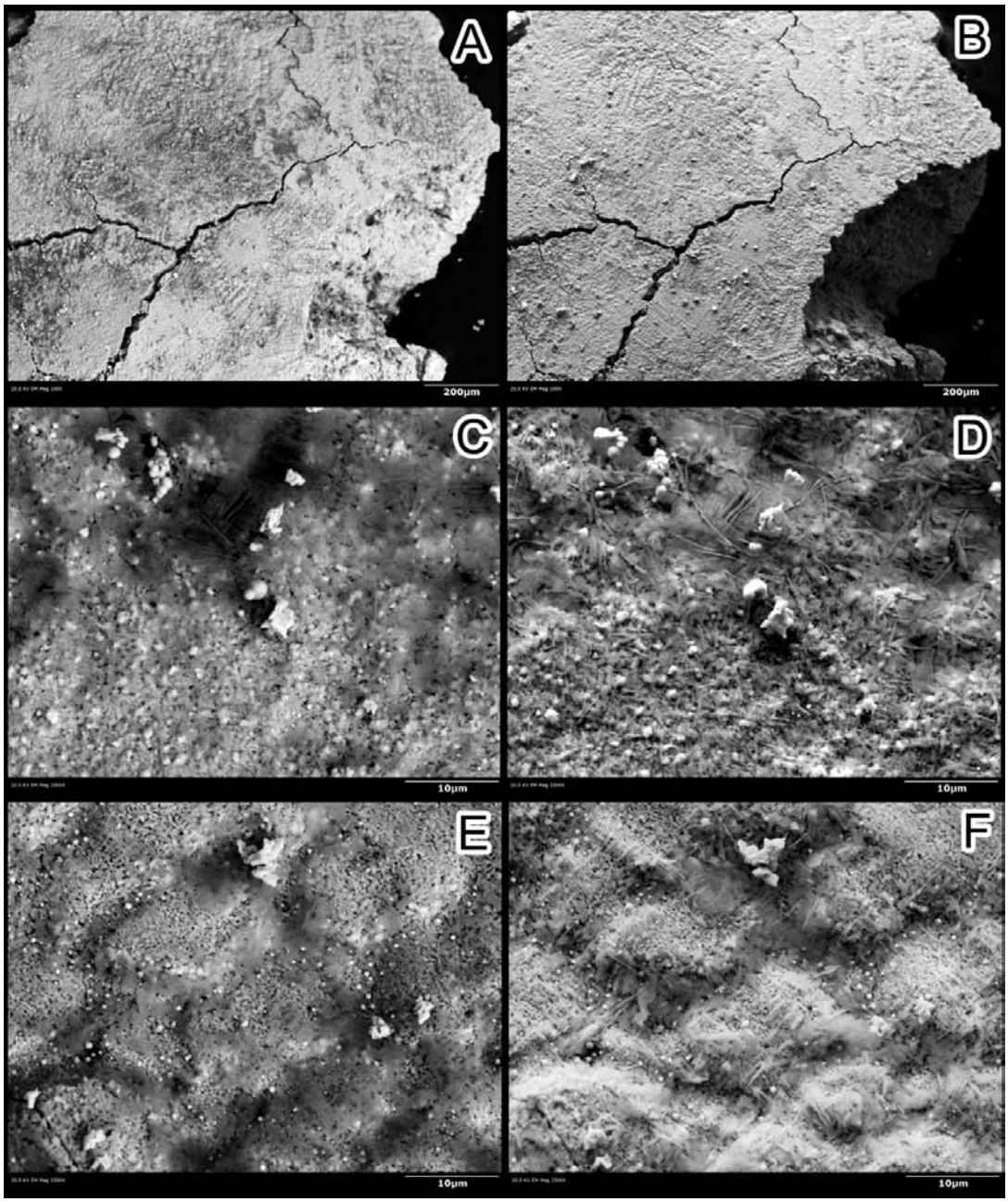

Figure 5. Micrographs of the surface of pellet 8 captured with SEM-BSE [A(100×), C(2500×) and E(2500×)] and SEM-SEI [B(100×), D(2500×) and F(2500×)].

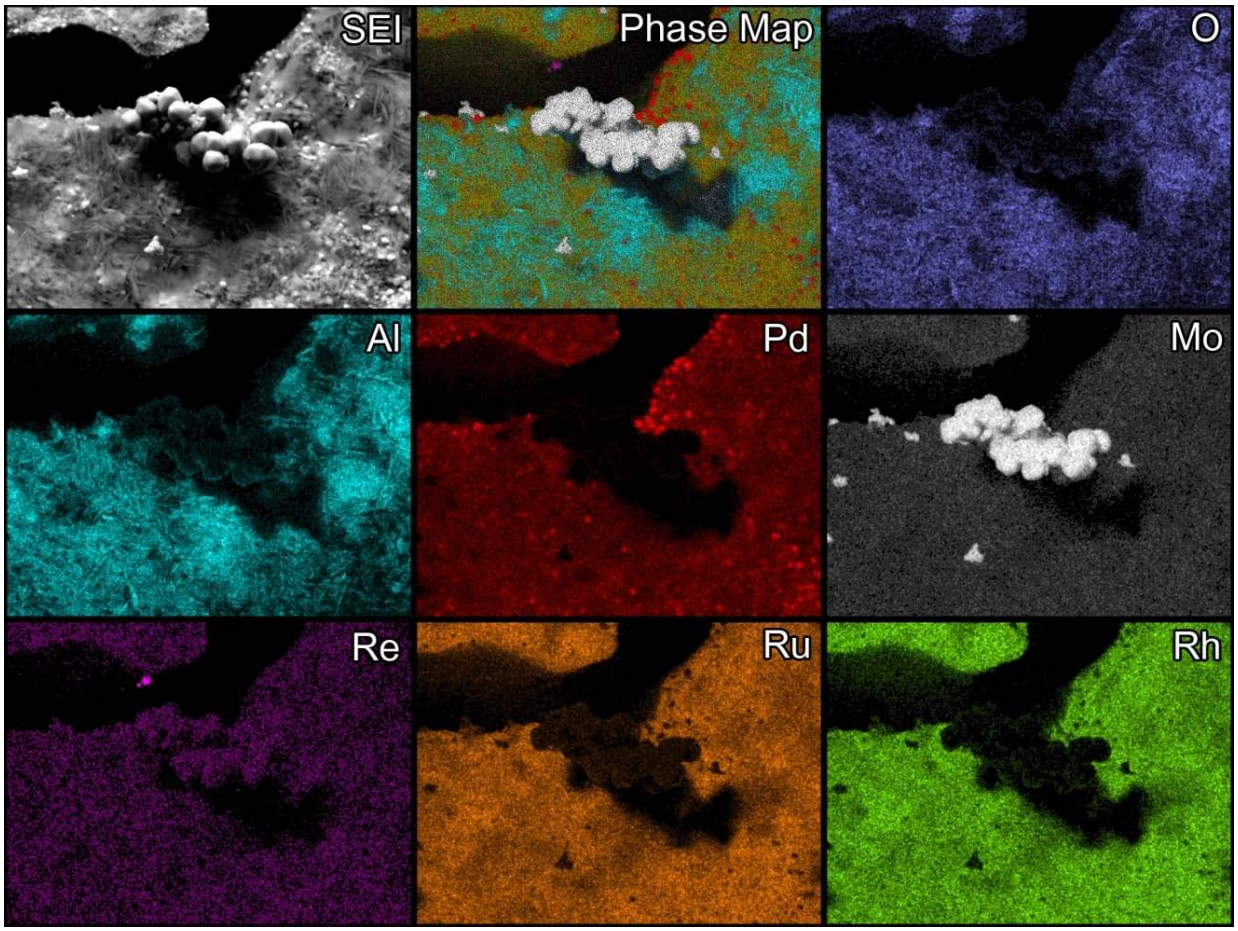

Figure 6. Elemental EDS dot map of pellet 8 after DSC-TGA experiment (ramp 5°C/min up to 900°C).

Following SEM-EDS analysis, the specimen was examined with XRD to determine the phases that resulted from the oxidation. Unfortunately, the specimen was only 18 mg and was scanned as a monolith to avoid destruction. Thus, the pattern shown in Figure 7 has weak reflections and, because the sample was not crushed to a powder, the diffraction pattern shows preferred orientation. The phases identified in the XRD pattern were similar to those identified with SEM-EDS. Palladium, Mo, and possibly Ru are identified as metals. The Pd structure is cubic, space group Fm-3m (225), which was the closest match; however, Ru and Rh also have the same structure with only slightly different unit cell sizes. The phase is likely an alloy of the three elements. Molybdenum forms a distinct structure that is also cubic with a space group of Im-3m (229). There is also one or more oxide phases tentatively identified as RhO_2, RuO_2, and/or PdO_2, all of which have the tetragonal structure P42/mnm (136). There was no clear sign of the ε-metal phase in the XRD pattern.

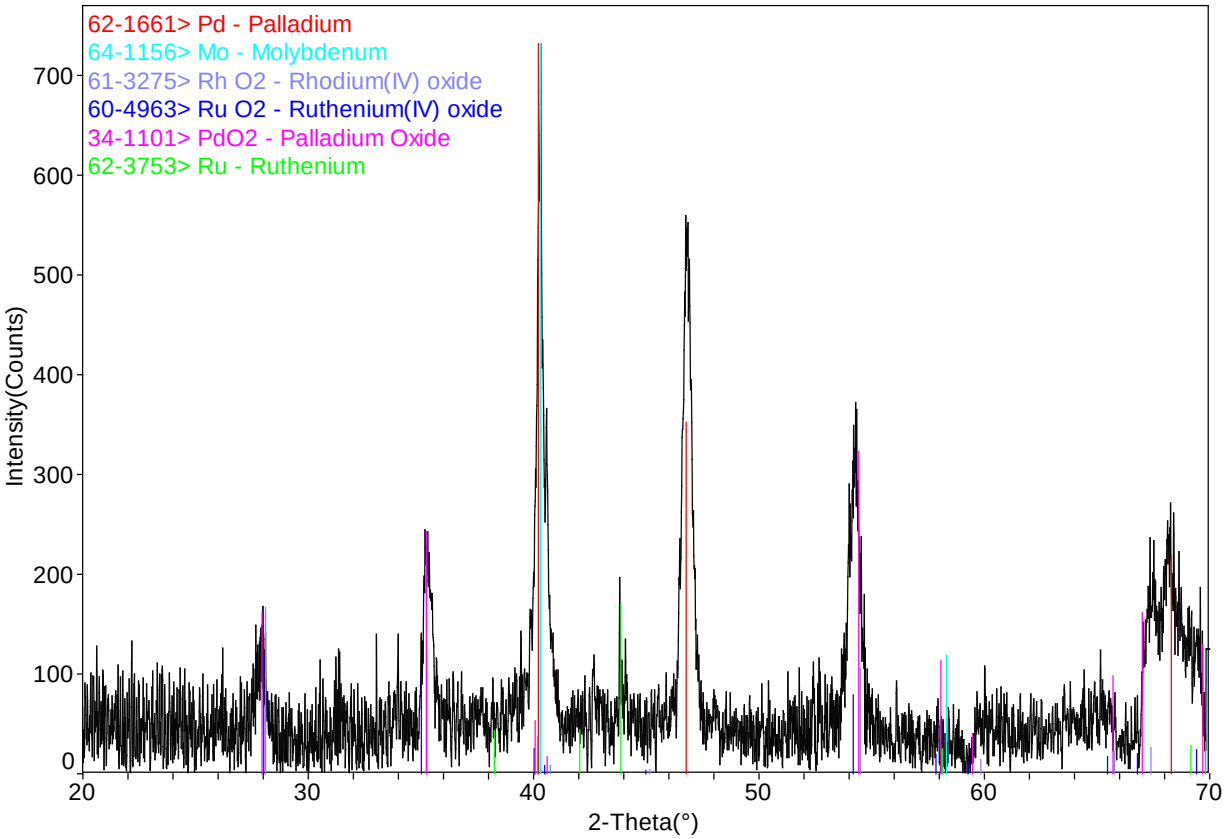

Figure 7. Background-subtracted XRD pattern from pellet 8 material after DSC-TGA experiment and with the phases identified.

3.2 Corrosion Testing

Electrochemical and SPFT testing were done to measure the corrosion rate for the ε-metal waste form. Electrochemical testing is commonly employed to quickly estimate the corrosion rate of metals by fitting the Tafel equation [Equation (1)] to the linear polarization data. However, the waste form qualification community and repository personnel are more familiar with corrosion tests such as the SPFT. The results of these two techniques are presented and compared. Note the results obtained here are preliminary because the experimental procedure for the electrochemical test was still under development. As the test protocol is developed, the corrosion rates reported here may be revised in the future and should only be taken as qualitative estimates.

3.2.1 Electrochemical Testing

Although we measured the OCP for the specimens described above, we do not report the results here. Instead the OCP measurements were used to reference the starting and end points of the linear polarization resistance measurements. The consensus of those working on the alloy waste form is that potentials should be referenced versus the potential of the (calomel) reference electrode and not the OCP measured in long term testing. This approach is planned for future studies. The OCP for these studies was ultimately obtained from the linear polarization measurements.

The results obtained by fitting the Stern-Geary equation [Equation (3)], or traditional Tafel equation [Equation (1)] to the linear polarization measurements (segment 4 of the protocol) conducted on each specimen in the series of solutions are summarized in Table 4. The Stern-Geary and Tafel were fit with

automatic selection of the fitting parameters in software (CorrView). In addition, the Tafel equation was calculated by manually selecting the anodic or cathodic data to determine β_a or β_c. An example of each fit to data is shown in Figure 8. See Appendix B to view the graphs and fits to the data shown in Table 4. The corrosion current is given as I_o at the voltage potential E_o for each specimen in each of the solutions. The estimated corrosion rates for the three specimens ranged from 0.4–2.8 µm/a with an mean of 0.8 µm/a [2.7×10^{-5} g/(m^2·d)] and a standard deviation of 0.4 µm/a for all of the test solutions, with the minimum rate occurring in the basic solution and the maximum occurring in either the brine or acidic + brine solutions. However, the cathodic branch was found not to be useful in the Tafel analysis. The tests conducted in the inert solution were done with an expanded cathodic range (0.3V below the OCP). In the future, the cathodic data range of the linear polarization test will be increased to 0.3 V below the calomel reference electrode voltage.

The standard deviation of the electrochemical measurements is quite high. One reason for this variability could be the sample surface before the test. Samples were final polished with 600-grit silicon carbide sand paper, the grit size of which is known to decrease by the minute on hard surfaces such as glass or ceramics. The ε-metal is a hard surface compared to most metals. For example, it cannot be filed with a standard hardened steel file. In future tests, diamond impregnated platens might provide consistent abrasive surface resulting in a more consistent surface finish between different samples, hence, more consistent dissolution data.

Optical micrographs taken after the electrochemical tests (Figure 9a-d), show distinct corrosion patterns. Red is the most corroded part of the specimen and white is the least corroded. This pattern occurs similarly irrespective of the solution chemistry, but is most distinct when the solution contains NaCl alone or in combination with the other chemicals. These micrographs qualitatively confirm the estimated corrosion rates determined from the Tafel fits.

Table 4. Fitted parameters determined by traditional Tafel fit to polarization resistance data.

		Stern-Geary, Auto fit				Tafel, Auto fit					Tafel, Manual fit				
Pellet #	Solution	*Rp* (Ω/cm^2)	*Io* (A/cm^2)	*Eo* (V)	Corrosion (μm/yr)	βa (mV)	βc (mV)	*Io* (A/cm^2)	*Eo* (V)	Corrosion (μm/yr)	βa (mV)	βc (mV)	*Io* (A/cm^2)	*Eo* (V)	Corrosion (μm/yr)
8	Basic + Brine	-1.6E+05	-2.4E-07	0.183	1.1	231.6	64.1	-1.2E-07	0.181	0.6	331.3	NA	1.7E-07	0.180	0.8
8	Acidic + Brine	-1.6E+05	-2.4E-07	0.289	1.2	176.1	50.4	-1.1E-07	0.287	0.5	183.6	NA	1.1E-07	0.286	0.5
8	Brine	-1.8E+05	-2.1E-07	0.155	1.0	193.7	35.2	-7.4E-08	0.152	0.4	323.1	NA	1.3E-07	0.152	0.6
8	Basic	-8.2E+05	-4.7E-08	0.171	0.2	162.9	65.6	-3.1E-08	0.170	0.2	334.1	NA	7.6E-08	0.169	0.4
8	Acidic	-4.9E+05	-7.8E-08	0.335	0.4	133.0	46.7	-3.4E-08	0.334	0.2	340.1	NA	1.4E-07	0.331	0.7
8	Inert*	-9.5E+04	-4.0E-07	0.029	2.0	1.9E+07	142.7	-5.8E-07	0.027	2.8	600.7	109.4	3.0E-07	0.027	1.5
9	Basic + Brine	-3.2E+05	-1.2E-07	0.204	0.6	164.9	45.2	-4.5E-08	0.202	0.2	330.0	NA	1.4E-07	0.202	0.7
9	Acidic + Brine	-4.2E+05	-9.2E-09	0.343	0.0	115.6	58.0	-3.6E-08	0.342	0.2	361.6	NA	2.5E-07	0.340	1.2
9	Brine	-1.6E+05	-2.3E-07	0.185	1.1	203.2	34.0	-7.9E-08	0.182	0.4	273.5	NA	1.1E-07	0.182	0.5
9	Basic	-1.0E+06	-3.8E-08	0.151	0.2	140.1	57.2	-2.0E-08	0.149	0.1	276.2	NA	5.8E-08	0.148	0.3
9	Acidic	-2.0E+05	-1.9E-07	0.285	0.9	105.8	24.0	-4.8E-08	0.283	0.2	177.2	NA	1.1E-07	0.283	0.5
9	Inert	-1.2E+05	-3.2E-07	0.051	1.6	298.4	42.3	-1.4E-07	0.049	0.7	276.0	NA	1.3E-07	0.049	0.6
9	Inert*	-1.9E+05	-2.0E-07	-0.063	1.0	469.2	165.2	-2.8E-07	-0.063	1.4	112.2	199.1	1.3E-07	-0.068	0.6
10	Basic + Brine	-1.2E+05	-3.1E-07	0.206	1.5	247.4	52.5	-1.5E-07	0.204	0.7	381.4	NA	2.1E-07	0.204	1.0
10	Acidic + Brine	-7.8E+04	-4.9E-07	0.308	2.4	238.4	57.0	-2.5E-07	0.306	1.2	249.2	NA	2.6E-07	0.306	1.2
10	Brine	-1.0E+05	-3.8E-07	0.159	1.8	256.7	50.3	-1.7E-07	0.157	0.8	306.8	NA	2.0E-07	0.156	1.0
10	Basic	-8.2E+05	-4.7E-08	0.143	0.2	179.9	56.7	-2.7E-08	0.141	0.1	262.4	NA	4.1E-08	0.140	0.2
10	Acidic	-1.9E+05	-2.0E-07	0.278	1.0	152.7	52.1	-8.7E-08	0.276	0.4	214.6	NA	1.4E-07	0.276	0.7
10	Inert*	-1.5E+05	-2.6E-07	-0.085	1.3	246.7	106.4	-1.9E-07	-0.086	0.9	937.3	97.4	3.9E-07	-0.129	1.9
10	Inert*										937.3	not fit	4.4E-07	-0.086	2.1
10	Inert*										not fit	97.4	1.4E-07	-0.086	0.7

*Indicates polarization resistance scanned from -0.3V to +0.5V relative to the OCP. All other scans were from -0.03V to +1V relative to the OCP. NA means insufficient data to manually fit cathodic side

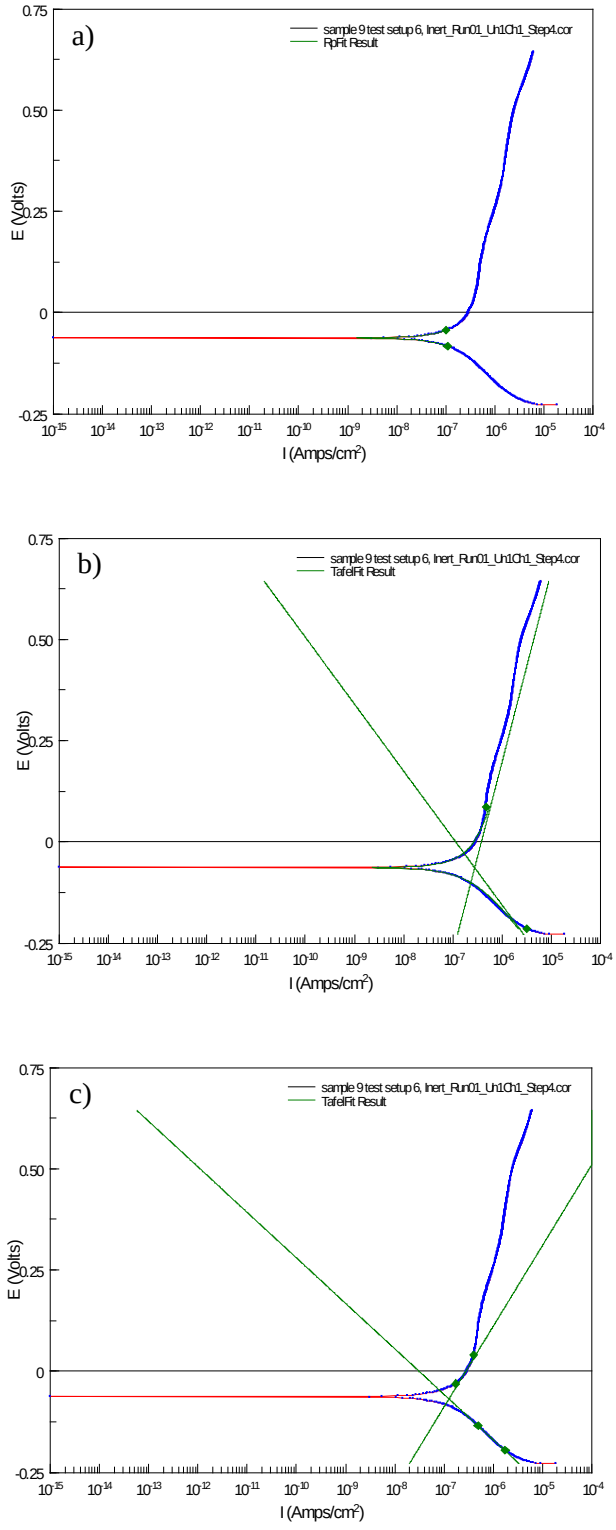

Figure 8 Linear polarization measurement of Pellet #9 in inert solution a) Stern-Geary fit, b) Tafel (auto), b) Tafel (manual anodic + cathodic). See Appendix B for additional graphs.

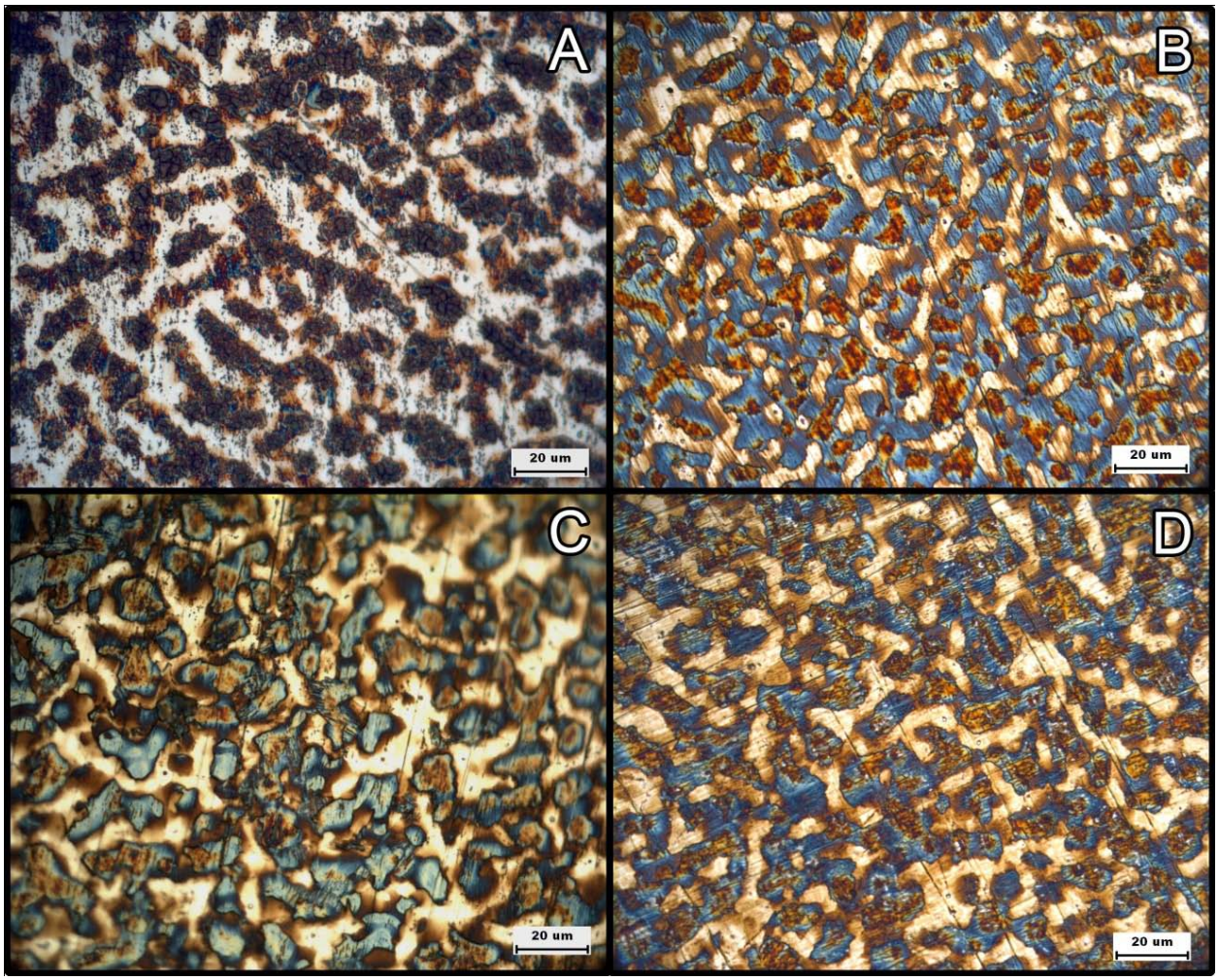

Figure 9. Optical micrographs post-electrochemical testing at 1000× (polarized reflected light); a) pellet 8 (H_2SO_4); b) pellet 9 (NaCl); c) pellet 8 (H_2SO_4+NaCl); and d) pellet 8 (NaOH+NaCl).

An elemental dot map of pellet 10, after electrochemical testing in NaOH + NaCl solution, is shown in Figure 10. This dot map was collected at low accelerating voltage of 6 kV to examine chemistry while limiting beam penetration depth to ~ 150 nm. This allows us to determine if a thin layer of oxide is present on the surface; high accelerating voltages would yield confounding results at best. Molybdenum and Pd are concentrated in the same regions of the sample while Re, Ru, and Rh appear fairly uniform across the map with dark regions corresponding to the highest Mo and Pd. The O map shows a similar but more distinct pattern where O is most concentrated in the regions opposite the Mo and Pd. This does not necessarily mean that oxidation is only occurring at these locations indicated on elemental map. It is likely that it occurs in the Mo-Pd rich regions as well, but may dissolve into solution as an oxide based on the SPFT results (see Section 3.2.2 below). Although weakly indicated, Re is also located in these areas. These data are consistent mechanistically with the SPFT results, but the corrosion rate is different than that measured with the SPFT method (see Section 3.2.2 below).

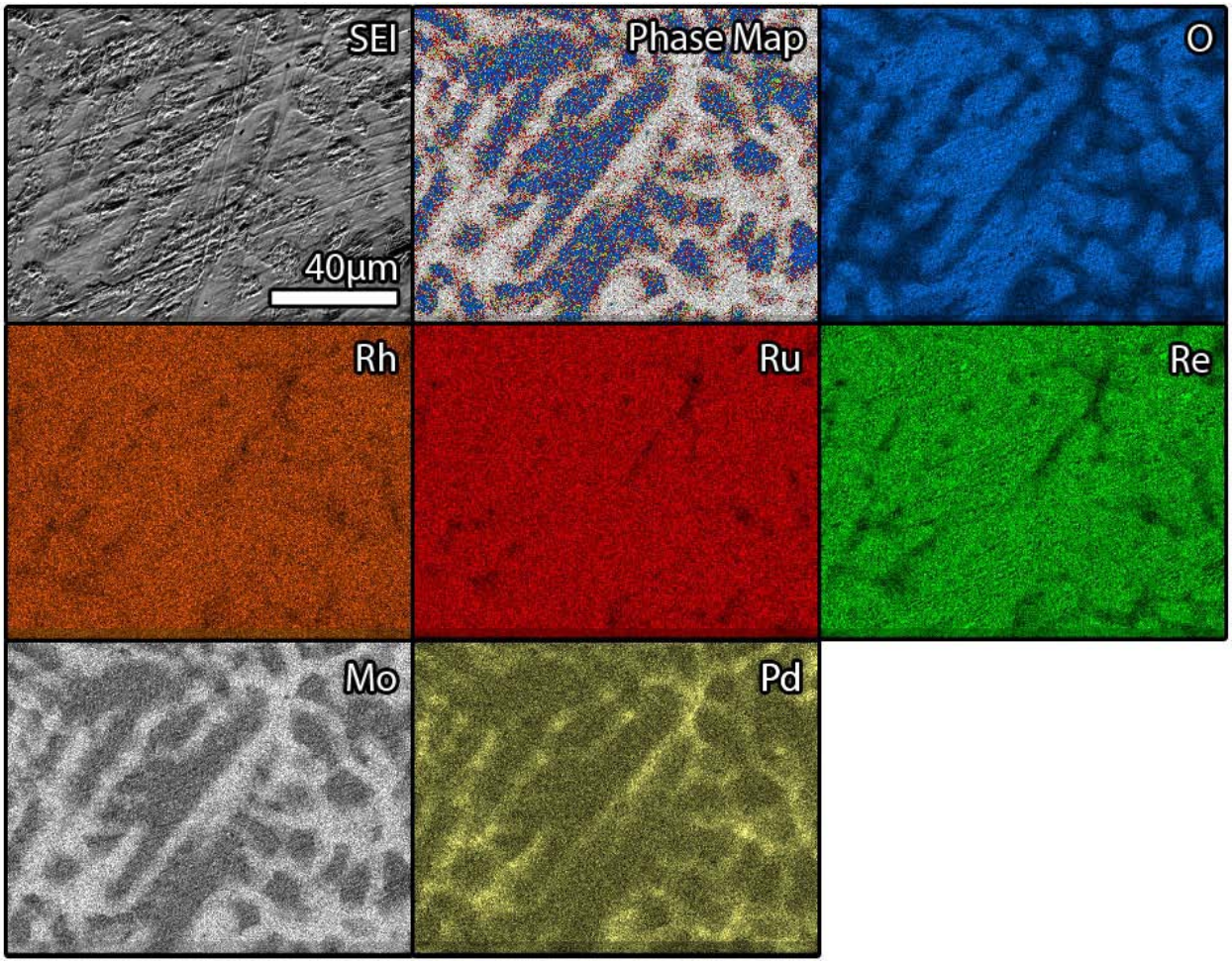

Figure 10. Elemental dot map of pellet 10 after electrochemical testing in NaOH+NaCl solution (phase map shows only the most concentrated element per pixel). The scale-bar shown in "SEI" micrograph (top left) is representative for all micrographs.

3.2.2 Single-Pass Flow Through Tests

The SPFT tests were initiated on the ε-metal phase coupons pellet 5-1, 5-2, and 25%-Re. The coupons were performed at a flow rate of 10 mL/day at 90 °C. Figure 11 presents the dissolution results from pellet 5-1 coupon. The dissolution rate was calculated from the concentration of Mo and Re in the effluent solution. The concentrations of Pd, Rh, and Ru were below the detection limits of the instrument, so dissolution rate calculations based on those elements were not performed. At pH 2.5, the dissolution rate of Mo started at 3.13×10^{-3} g/(m^2·d) and gradually reduced to 4.32×10^{-4} g/(m^2·d) after 49 days.[b] The concentration then decreased further before stabilizing at 1.94×10^{-4} g/(m^2·d) after 220 days and remaining at steady state for a further 100 days. The initial Re dissolution rate was 1.07×10^{-3} g/(m^2·d)

[b] For non-metallic samples, high initial rates are associated with high-energy surfaces that dissolve quickly and allow the dissolution rate to approach steady state. We assume that the same effect is taking place here.

and gradually decreased to 2.58×10^{-4} g/(m^2·d) after 49 days. It remained at that concentration for 322 days.

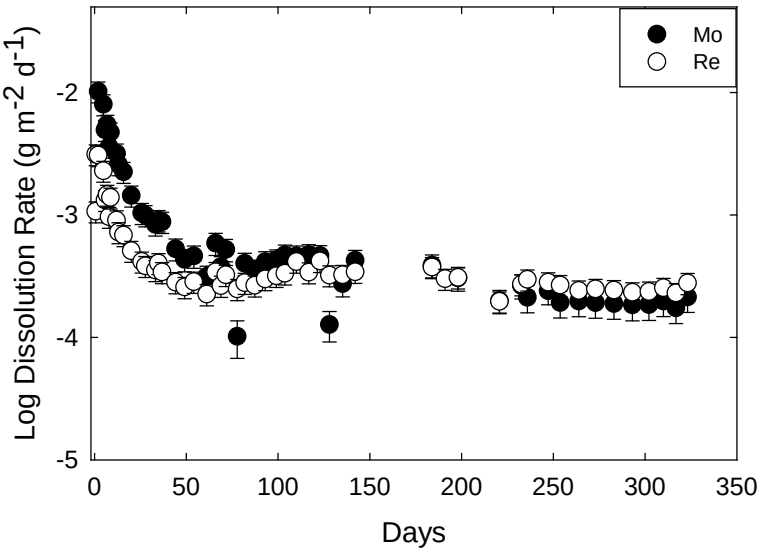

Figure 11. Dissolution results of pellet 5-1 single-pass flow through after 323 days.

Figure 12 presents the results from the pellet 5-2 coupon over time. Similar to the pellet 5-1 case, the dissolution rate was calculated from Mo and Re aqueous concentrations. At pH 9.0, the dissolution rate for Mo started at 3.99×10^{-2} g/(m^2·d) and decreased to 5.20×10^{-4} g/(m^2·d) after 72 days, where it remained at steady state. The Re dissolution started at 1.39×10^{-2} g/(m^2·d) and decreased to 4.84×10^{-4} g/(m^2·d) after 72 days, where it remained at steady state.

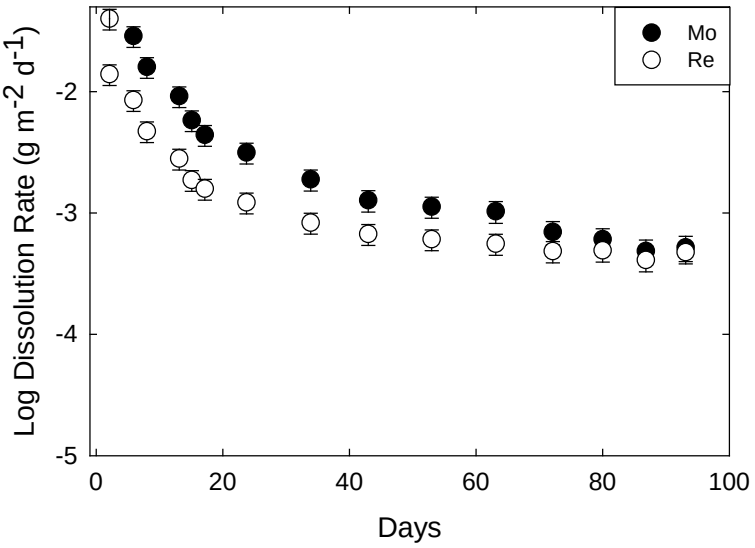

Figure 12. Dissolution results of pellet 5-2 single-pass flow through after 93 days.

Figure 13 presents the results from the pellet 25%-Re coupon. Aqueous concentrations of Mo and Re were used to calculate the dissolution rate. At pH 7.0, the dissolution rate for Mo started at 1.35×10^{-2} g/(m^2·d) and decreased to 1.15×10^{-4} g/(m^2·d) after 60 days, where it remained at steady state. The dissolution rate of Re started at 1.06×10^{-2} g/(m^2·d) and decreased to 4.9×10^{-5} g/(m^2·d) after 71 days. It reached a steady dissolution rate of 9.54×10^{-5} g/(m^2·d) at 88 days.

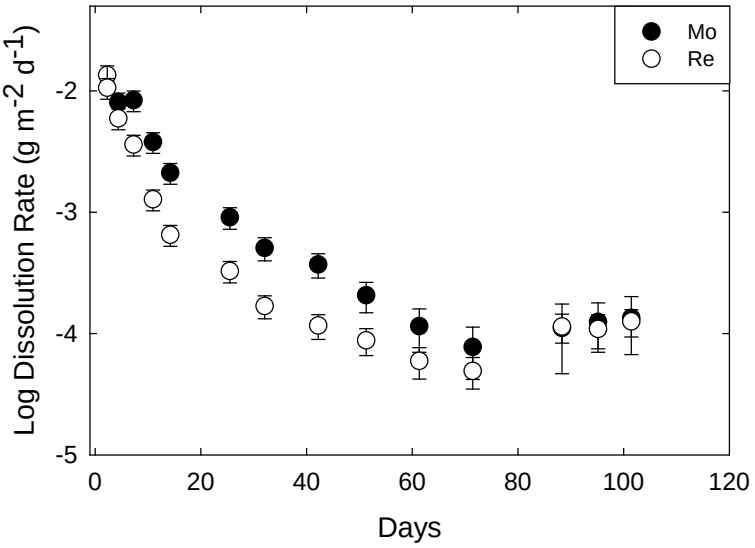

Figure 13. Dissolution results of pellet 25%-Re SPFT after 105 days.

Results from the preliminary SPFT tests on the ε-metal phase are summarized in Table 5 and indicate that dissolution is slightly increased at pH 9.0 compared to pH 2.5 [5×10^{-4} compared to 2×10^{-4} g/(m^2·d)], based on the Mo release rates. However, this could be within experimental error taking the errors in measuring the surface area into account. Results from the pellet 25%-Re coupon at pH 7.0 were the lowest at 1.2×10^{-4} g/(m^2·d); however, because the composition of the coupon was slightly different compared to the coupons 5-1 and 5-2 (Table 1), a direct comparison cannot be made on pH alone. At the same pH value, the dissolution rates are the same for Mo and Re within the projected uncertainty of ±35% RSD. The dissolution rate appears to be nearly pH independent from strongly acidic (pH = 2.5) to neutral (pH = 7). Although the dissolution rate appears to increase above pH 7, the increase is insufficiently strong to say that it increases with any certainty. To obtain results that can be used to compare materials of different composition and at different pH values, more experiments are planned. In particular, a set of experiments in which the *q*/*S* (flow rate/surface area) is varied to make sure that each material is being tested under conditions where no back reactions occur; reactions that can decrease the concentration in solution relative to another material. These tests will be performed in the future.

It should be noted that these tests were performed to obtain the highest dissolution rates. By way of comparison, these dissolution rates are approximately those expected from borosilicate glass ***at the final (long-term) rate***. Typical forward dissolution rates for borosilicate glasses are in the range of 0.1 g/(m^2·d). Thus, the rates measured to date for ε-metal, albeit preliminary, are about 1000 times less than those of borosilicate glasses.

Table 5. Results from the SPFT tests on ε-metal specimens at different pH values and 90 °C

Sample	pH(25 °C)	Dissolution Rate, 10^{-4} g/(m^2·d)	
		Mo	Re
5-1	9.0	5.20	4.84
5-2	2.5	1.94	2.58
25%-Re	7.0	1.15	0.954
Average		2.8	2.8

The surface of specimen, pellet 5-1, was analyzed with SEM/EDS following the SPFT test. Figure 14 shows SEM-SEI micrographs of the surface at 90×, 250×, 750×, and 900× magnifications. The surface clearly shows signs of etching deduced from the more defined microstructure than were observed in similar samples examined before the SPFT test. In addition, Figure 14d shows small, dimple patterns that do not appear to correlate with the grain boundaries. Elemental spot EDS analysis was done at low (6 kV) and high (15 kV) accelerating voltages (locations shown in Figure 15) to examine concentrations versus depth, with the results given in Table 6. Oxygen was observed as dark features in Figure 14 and Figure 15 at 6 kV accelerating voltage. At 15 kV, the composition of the metal dominates the EDS spectrum. This indicates the oxide layer was quite thin because the estimated beam penetration depth was 155 nm at 6 kV and 715 nm at 15 kV. Carbon concentrations were less clear than O, as it was seen in most areas at low accelerating voltage, which likely indicates that the surface was contaminated with C or some C-bearing material.

An elemental dot map (Figure 16), collected at 6 kV, shows the distribution of ε-metal components (Mo, Re, Ru, Rh, and Pd) along with O, C, and a phase map. The phase map shows the dominate element at a given location. The phase map shows areas high in O, Re, and Mo related to the microstructure of the sample (before SPFT). This map clearly shows oxidation mainly in regions slightly poor in Mo and Re. However, Mo and Re are observed in the effluent, which indicates that both oxidize and are soluble oxides. This explains the lack of O in those regions. Whereas, elements Pd, Rh, and Ru are below detection limits: because while they do oxidize, these oxides are insoluble, or at least undetectable in solution. It is also possible these three metals reform on the surface of the specimen. Examination of the raised areas (1 and 2 in Figure 15) show that, for the most part, these particles precipitated on the surface as evidenced by the discontinuity of the polishing scratches that were on the original surface of the specimen. This behavior is not found in the specimens from the electrochemical testing. . Perhaps unrelated, but interesting in this context, is the observation that Mo metal condenses (reforms) on the surface of the oxidizing metal (Section **Error! Reference source not found.**; Figure 6).

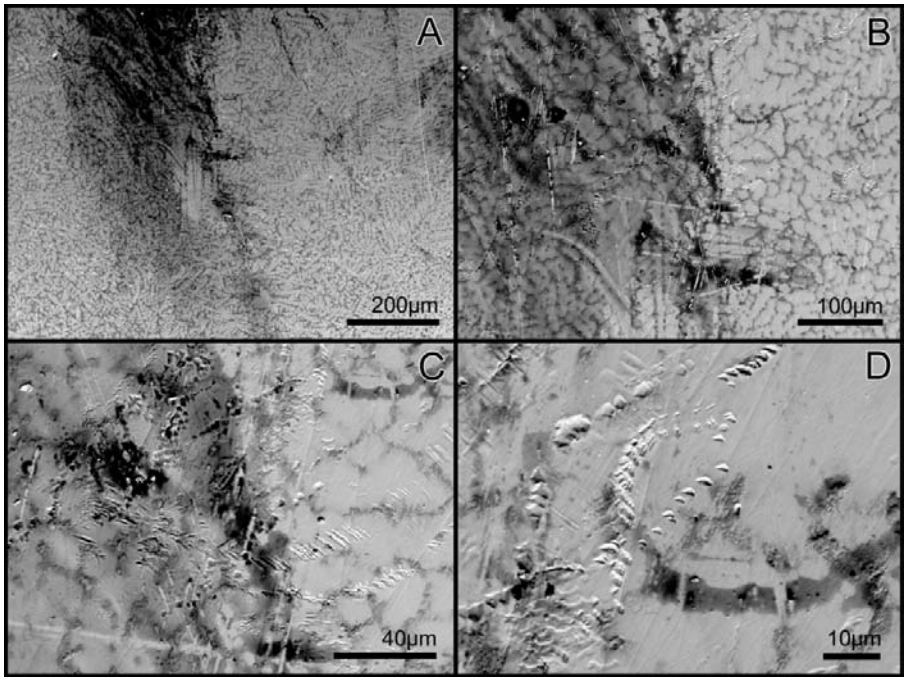

Figure 14. SEM-SEI micrographs of pellet 5-1 surface after SPFT test: a) 90×, b) 250×, c) 750×, and d) 900×.

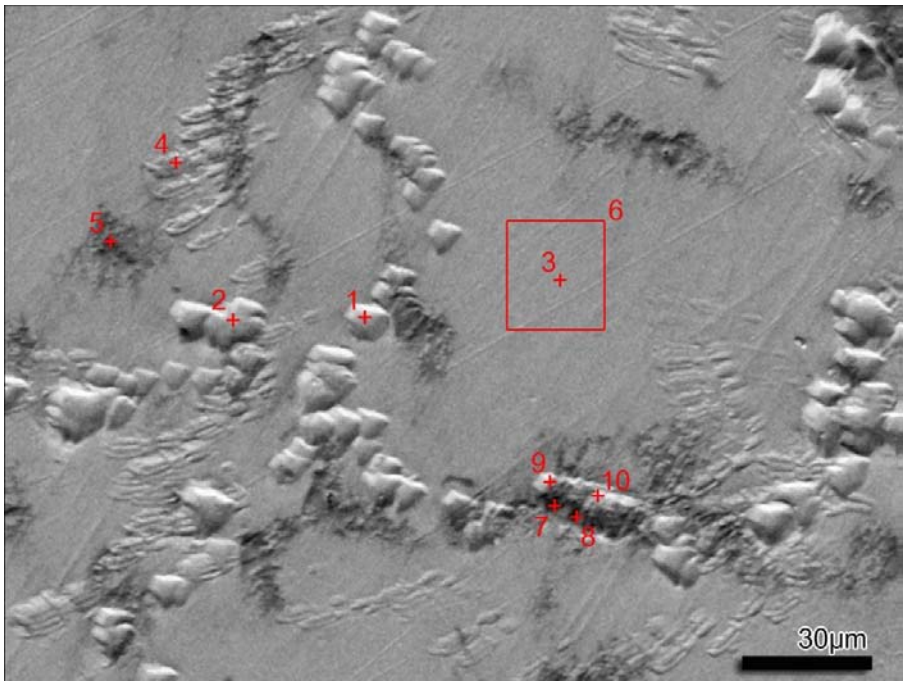

Figure 15. SEM-SEI micrograph (900×) with EDS spot/area locations.

Table 6. Normalized elemental analyses of pellet 5-1 sample surface post-SPFT at accelerating voltage of 6 and 15 kV, mole%. See Figure 15 for spot locations.

Location	1	2	3	4	5	6a	6b	7a	7b	8a	8b	9a	9b	10a	10b
kV	6	6	6	6	6	6	15	6	15	6	15	6	15	6	15
C	14	17	10	7	7	6		15	5	13	5	16	1	18	
O				29	55			46		52				32	
Mo	40	38	38	30	8	41	43	7	34	8	35	40	43	21	46
Ru	27	25	29	22	18	31	33	20	29	19	30	27	23	18	24
Rh	7	4	7	3	3	6	4	4	5	2	6	1	5	2	5
Pd		6		4	7		6	8	24	5	22	7	24	7	20
Re	13	11	16	6	1	16	15		3	1	3	8	3	3	5

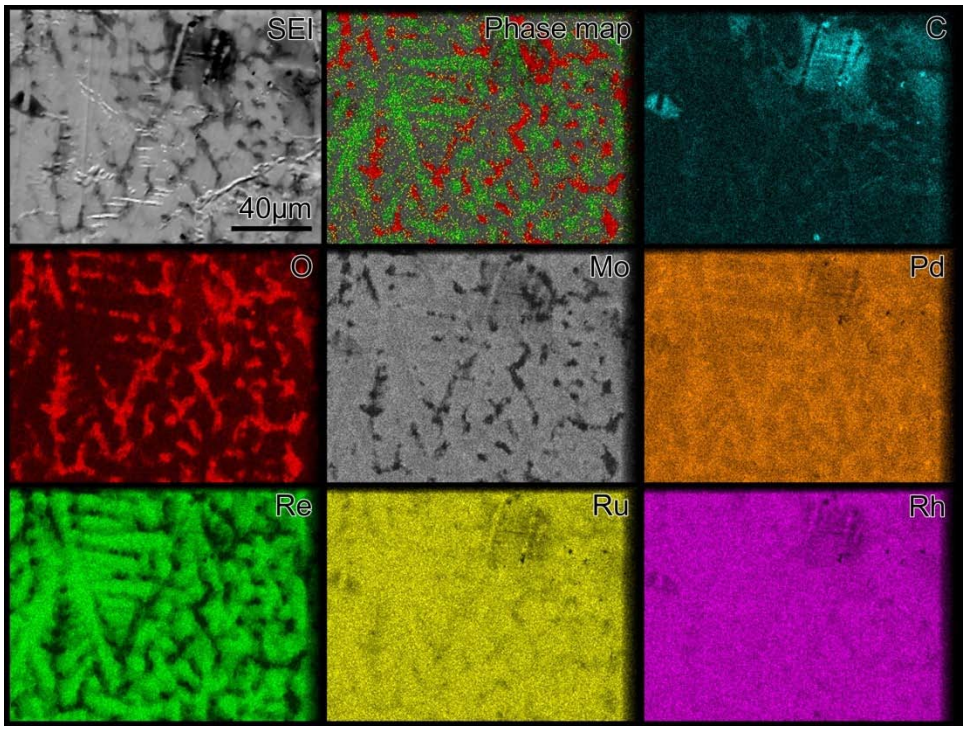

Figure 16. EDS dot map of pellet 5-1 surface after SPFT test showing elemental distribution.

3.3 Evaluation of ε-metal Commercial Processing Methods

Evaluation of two of the three top commercial processes (Rohatgi and Strachan 2011) for fabrication of the ε-metal phase, namely microwave sintering and spark plasma sintering, are underway. A commercial vendor has not been selected for the third (hot isostatic pressing). To date, three samples (pressed pellets containing the five metals that compose ε-metal) of the ε-metal have been sent for processing with spark-plasma sintering and microwave sintering. Thus far, we have only received the microwave sintered samples from the vendor (Figure 17). Therefore, comparisons cannot be made at this point; however, some initial characterization of the microwave samples has been done.

The as-received microwave sintered samples were examined with OM (Figure 17). Each pellet was about 23 mm in diameter and several phases were observed. Colors of these phases varied from a dark grey/brown at the perimeter to dark and light blue rings (oxidation) inside the perimeter to lighter regions towards the center. In Microwave-3, a small cubic crystal (~ 10 µm) was observed.

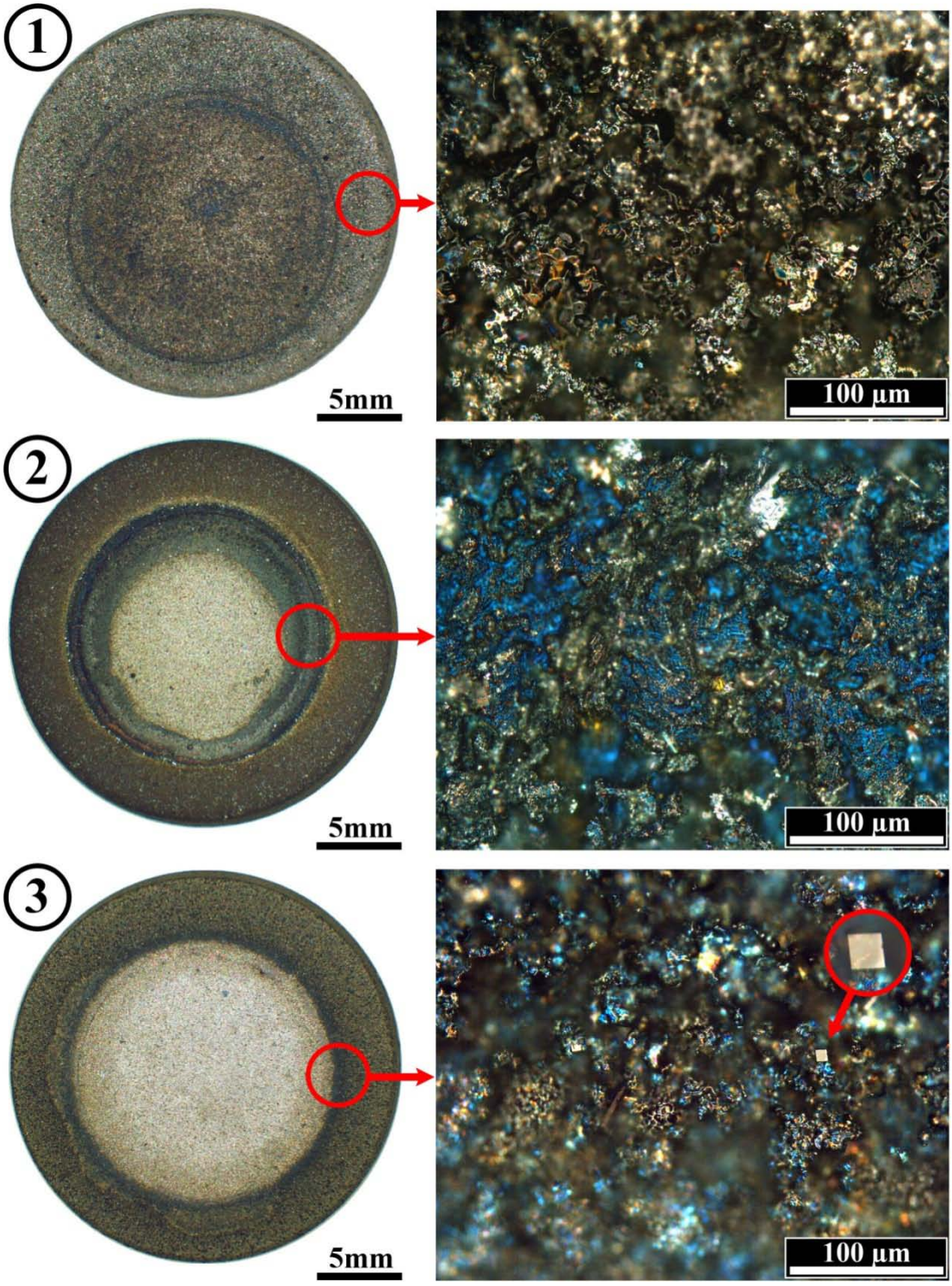

Figure 17. Optical micrographs of the microwave-sintered ε-metal pellets.

The specimen surfaces were then analyzed as received with XRD in monolithic form to determine the phase assemblage at the surface. Table 7 shows that the phases consisted of two hexagonal phases with P63/mmc space group, which is the same as ε-metal, as major phases (Epsilon #1 and #2) and two with cubic structures as minor phases (Cubic #1 and #2). The unit cell dimensions of Epsilon #1 remain fairly

constant between the three pellets, while the c-axis of Epsilon #2 differs significantly from Micro #1 (41.9 nm) to Micro #2 and Micro #3 (44.2, 44.3 nm, respectively). The unit cell dimensions of the cubic phases also differ significantly between the three samples. Figure 18 shows the pattern obtained from whole pattern fitting for the Micro #3 sample. The ε-metal alloy (Epsilon #1) dominates the patterns followed by Epsilon #2 and trace amount of Cubic #2.

Because we do not have ε-metal powder (it is very hard to make in uniform and small particle sizes), we have to be content with sending pellets or powder specimens consisting of the five constituent metals. Since we are just trying to evaluate the capability to consolidate the ε-metal, this approach is sufficient for now. However, in the future, we may need to produce a large billet of ε-metal and have a spherical powder made from it, such as by spin atomization. This is expensive as it requires a billet weighing several kilograms.

Table 7. Results from the semi-quantitative XRD analyses of the microwave-sintered ε-metal pellets

Phase	Space Group	Unit Cell Dimension, nm		Amount of each phase, mass%		
		a	c	micro #1	micro #2	micro #3
Epsilon #1	P63/mmc	27.6	44.2-44.3	61	57	75
Epsilon #2	P63/mmc	27.4-27.7	40.9-41.9	31	29	23
Cubic #1	Fm-3m	38.9-35.3	--	5	11	0
Cubic #2	Fm-3m	41.3-40.4	--	2	4	3

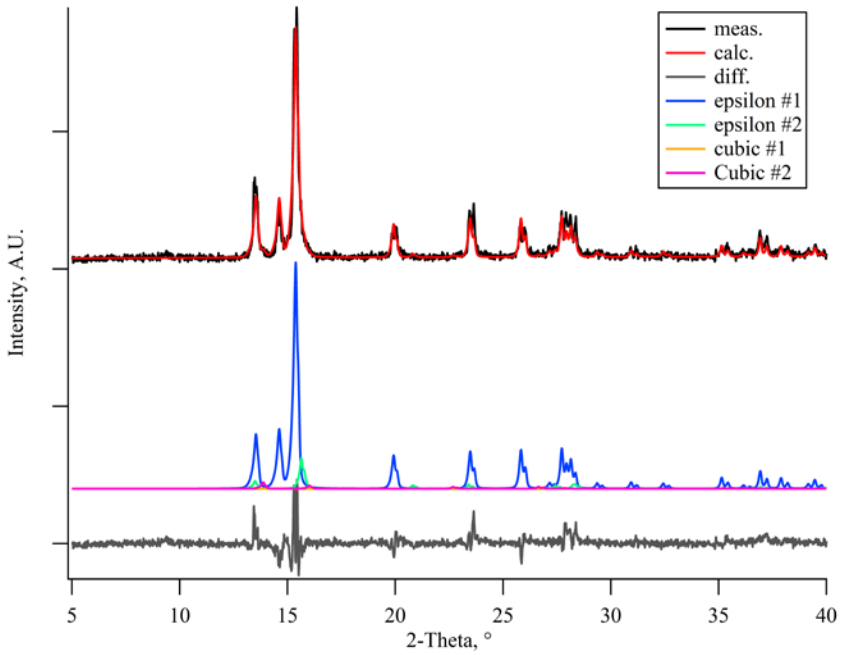

Figure 18. Whole pattern fitting to micro #3 XRD pattern with measured, calculated, difference, and phases patterns shown.

Specimen densities were also determined with the Archimedes method in ethanol. After letting the pellets de-air in ethanol for the density measurement, the Micro #1 sample turned the ethanol a dark blue color. The blue ethanol solution was archived and will be analyzed in FY 2012 to determine the cause of the blue color. However, Mo(VI) compounds are usually a very intense blue. The results of the density measurements are given in Table 8. The densities of the microwave sintered specimens were much lower than expected; this indicates there was basically no consolidation during the sintering process.

Table 8. Microwave sintering firing parameters, measured density, and % theoretical density (12.12×10^3 kg/m^3 obtained with arc melting).

Sample	Sintering Temperature, °C	Hold Time, min	Density, 10^3 kg/m^3	
			Measured	Theoretical, %
Micro #1	1400	45	6.98	57.6
Micro #2	1450	43	6.92	57.1
Micro #3	1500	43	7.09	58.5

4. CONCLUSIONS

The data obtained during FY 2011 indicate the ε-metal phase is chemically durable. The arc melted specimens show there are two phases with the same structure P63/mmc (hexagonal) and nearly identical unit cell dimensions. One of the phases is rich in Pd and the other Mo and Re. These two phases appear to behave differently during dissolution in electrochemical and SPFT tests. The dissolution rates for these specimens as measured with the SPFT test appear to be independent of pH and composition, although these are preliminary results. The average dissolution rate of 2.8×10^{-4} g/(m^2·d) is about 1000 times less than the dissolution rate of a typical borosilicate glass for nuclear waste. Electrochemical tests suggest that the corrosion rates are approximately the same irrespective of the solution in which the test is carried out. The average corrosion rate as measured electrochemically on three pellets of nominally the same composition is 0.8(0.4) μm/y [2.7×10^{-5} g/(m^2·d)]. The dissolution rates for other metal alloy waste forms are similar at ~5 and ~0.2 μm/a at pH values of 2 and 9, respectively (Ebert 2005). The response to pH changes is also small above a pH of 4. Typical corrosion rates measured at alkaline pH values for container materials for waste forms are <1 μm/y (Kursten et al. 2011; Winsley et al. 2011). Characterization of test specimens after testing indicates the dissolution is complex and involves oxidative dissolution followed by precipitation of both oxide and metallic phases. These data suggest preferential dissolution of the Mo-Re-rich phase over the Pd-rich phase. However, this is further complicated by the precipitation of both metallic and oxide phases. More dissolution and electrochemical tests are needed to determine the dissolution mechanism(s).

Oxidation of two ε-metal specimens shows that the material first gains mass (oxide formation) then loses mass loss as the oxides volatilize. Not all of the metal is oxidized and not all of the oxides are lost. Some Mo appears to form as metallic clusters during the oxidation process. The principal mass loss appears to be oxides of Mo and Re.

Several commercial processes for the consolidation of the ε-metal phase were identified by Rohatgi and Strachan (2011). Vendors for two of these—microwave sintering and spark plasma sintering—were identified this fiscal year and samples sent to them for testing. The vendor for microwave sintering completed sample preparation/consolidation and returned the specimens to PNNL. Characterization of these specimens showed that at 1550 °C, the original five metals (Mo, Pd, Re, Rh, and Ru) had reacted sufficiently to be nearly converted to ε-metal. The sintered densities were about 50% of the theoretical density, however. A set of three metallic pellets was sent to a vendor for spark plasma sintering. These specimens have yet to be returned. We have not yet identified a vendor for the third promising technology (hot isostatic pressing).

5. REFERENCES

ASTM. 2010. "*Astm C1662 - 10 Standard Practice for Measurement of the Glass Dissolution Rate Using the Single-Pass Flow-through Test Method.*" American Society for Testing and Materials, West Conshohocken, PA.

Cui, D, J Low, CJ Sjostedt, and K Spahiu. 2004. "On Mo-Ru-Tc-Pd-Rh-Te Alloy Particles Extracted from Spent Fuel and Their Leaching Behavior under Ar and H-2 Atmospheres." *Radiochimica Acta* 92(9-11):551-55.

Ebert, WL. 2005. *Testing to Evaluate the Suitability of Waste Forms Developed for Electrometallurgically Treated Spent Sodium-Bonded Nuclear Fuel for Disposal in the Yucca Mountain Reporsitory*. . Report No. ANL-05/43, Argonne National Laboratory, Argonne, IL.

Gauthier-Lafaye, F, P Holliger, and PL Blanc. 1996. "Natural Fission Reactors in the Franceville Basin, Gabon: A Review of the Conditions and Results of a "Critical Event" in a Geologic System." *Geochimica et Cosmochimica Acta* 60(23):4831-52.

Goode, JH, and RG Stacy. 1978. *Head-End Reprocessing Studies with H.B. Robinson-2 Fuel*. Report.

Icenhower, JP, and PM Dove. 2000. "The Dissolution Kinetics of Amorphous Silica into Sodium Chloride Solutions: Effects of Temperature and Ionic Strength." *Geochimica et Cosmochimica Acta* 64(24):4193-203.

Icenhower, JP, PB McGrail, DM Strachan, RD Scheele, VL LeGore, EA Rodriguez, JL Steele, CF Brown, and MJ O'Hara. 2002. Experimental Determination of the Dissoution Kinetics of Plutonium- and Uranium-Bearing Ceramics at 90^{o}c. In *Proceedings of Material Research Society Symposium*, 433-40 pp.

Icenhower, JP, PB McGrail, J Weber, Walter J., BD Begg, NJ Hess, EA Rodriguez, JL Steele, CF Brown, and MJ O'Hara. 2000. Dissolution of $A_2ti_2o_7$ (a=Y^{3+}, Gd^{3+}, or Lu^{3+}) Pyrochlore by Experiment at Ph=2, T=90^{o}c: Evidence of Solubility Controlusing a Linear Free Energy Model. In *Proceedings of Material Research Society*, 397-403 pp.

Icenhower, JP, DM Strachan, MM Lindberg, EA Rodriguez, and JL Steele. 2003. *Dissolution Kinetics of Titanate-Based Ceramic Waste Forms: Results from Single-Pass Flow Tests on Radiation Damaged Specimens*. Report, Pacific Northwest National Laboratory, Richland, WA.

Jubin, RT, GD DelCul, JM Giaquinto, ES Meyers, DW Ramey, RS Owens, and BB Spencer. 2009a. Afci Fuel Reprocessing R&D: Performance of Coupled End-to-End Integrated Voloxidation and Dissolver Off-Gas Treatment. In *Proceedings of Global 2009*,

Jubin, RT, GD DelCul, JM Giaquinto, ES Meyers, DW Ramey, RS Owens, and BB Spencer. 2009b. Afci Fuel Reprocessing R&D: Performance of the Coupled End-to-End Integrated Voloxidation and Dissolver Off-Gas Treatment Systems. Presented at *Waste Management 2009*,

Kleykamp, H. 1985. "The Chemical-State for the Fission-Products in Oxide Fuels." *Journal of Nuclear Materials* 131(2-3):221-46.

Kleykamp, H. 1988. "The Chemical-State of the Fission-Products in Oxide Fuels at Different Stages of the Nuclear-Fuel Cycle." *Nuclear Technology* 80(3):412-22.

Kleykamp, H. 1989. "Constitution and Thermodynamics of the Mo-Ru, Mo-Pd, Ru-Pd, and Mo-Ru-Pd Systems." *Journal of Nuclear Materials* 167(1):49-63.

Kleykamp, H. 2005. "Highlights of Experimental Thermodynamics in the Field of Nuclear Fuel Development." *Journal of Nuclear Materials* 344(1-3):1.

Kleykamp, H, JO Paschoal, R Pejsa, and F Thummler. 1985. "Composition and Structure of Fission-Product Precipitates in Irradiated Oxide Fuels - Correlation with Phase Studies in the Mo-Ru-Rh-Pd and Bao-Uo_2-Zro_2-Moo_2 Systems." *Journal of Nuclear Materials* 130:426-33.

Kursten, B, F Druyts, DD Macdonald, NR Smart, R Gens, L Wang, E Weetjens, and J Govaerts. 2011. "Review of Corrosion Studies of Metallic Barrier in Geological Disposal Conditions with Respect to Belgian Supercontainer Concept." *Corrosion Engineering Science and Technology* 46(2):91-97. 10.1179/1743278210y.0000000022.

McGrail, BP. 1997. *Measurement of Waste Form Dissolution Kinetics Using a Single-Pass Flow-through Apparatus*. Accessed on February 3, 2000 at (last updated

McGrail, PB, and DK Peeler. 1995. *Evaluation of the Single-Pass Flow-through Test to Support a Low-Activity Waste Specification.* Report, Pacific Northwest Laboratory, Richland, WA.

Pierce, EM, JP Icenhower, RJ Serne, and JG Catalano. 2005. "Experimental Determination of Uo_2 (Cr) Dissolution Kinetics: Effects of Solution Saturation State and Ph." *Journal of Nuclear Materials* 345:206-18.

Rohatgi, A, and DM Strachan. 2011. *Potential Production Technologies for E-Metal, Tc, and Noble Metals – an Initial Assessment*. Report No. PNNL-20313, Pacific Northwest National Laboratory, Richland, WA.

Strachan, DM, JV Crum, EC Buck, BJ Riley, and MR Zumhoff. 2010. *Fiscal Year 2010 Summary Report on the Epsilon-Metal Phase as a Waste Form for ^{99}tc*. Report No. FCRD-WAST-2010-000188 (PNNL-19828), Pacific Northwest National Laboratory, Richland, WA.

Utsunomiya, S, and RC Ewing. 2006. "The Fate of the Epsilon Phase (Mo-Ru-Pd-Tc-Rh) in the Uo_2 of the Oklo Natural Fission Reactors." *Radiochimica Acta* 94(9-11):749-53. 10.1524/ract.2006.94.9.749.

Wellman, DM, JP Icenhower, AP Gamerdinger, and SW Forrester. 2006. "Effects of Ph, Temperature, and Aqueous Organic Material on the Dissolution Kinetics of Meta-Autunite Minerals, $(Na, Ca)_{2-1}[(Uo_2)(Po_4)]_2$ $3h_2o$." *American Mineralogist* 91:143-58.

Wellman, DM, JP Icenhower, and WJ Weber. 2005. "Elemental Dissolution Study of Pu-Bearing Borosilicate." *Journal of Nuclear Materials* 340:149-62.

Winsley, RJ, NR Smart, AP Rance, PAH Fennell, B Reddy, and B Kursten. 2011. "Further Studies on the Effect of Irradiation on the Corrosion of Carbon Steel in Alkaline Media." *Corrosion Engineering Science and Technology* 46(2):111-16. 10.1179/1743278210y.0000000010.

Wolery, TJ. 1992. *Eq3nr, a Computer Program for Geochemical Aqueous Speciation-Solubility Calculations: Theoretical Manual, User's Guide, and Related Documentation (Version 7.0)*. Report, Lawrence Livermore National Laboratory, Livermore, CA.

Appendix A

Interim Electrochemical Measurements Protocol

Electrochemical Measurements Protocol

1. Scope

This test method covers an experimental protocol for making a variety of electrochemical measurements on simulated alloy waste forms. The protocol includes many examples which are meant as guides to aid the researcher, but is not meant to be all inclusive.

2. Referenced Documents

ASTM G5-94

3. Significance and Use

4. Apparatus

a. Use gloves when handling all electrochemical cell equipment and making chemical mixtures to prevent contamination.

b. **Measurement solution preparation**

i. For test solutions use high purity reagent water and chemicals.
ii. Solutions in table 1 may be used to aid in interlaboratory comparisons.

Table 1. Electrolyte conditions and masses/volumes of reagents needed to attain mixture concentrations listed in table 1. Solutions will be tested both aerated and deaerated. (Source: AFCI-WAST-2010-000161). Example solution mixture directions can be found in the appendix.

Condition	Solution composition
Acidic	0.0001 mol/kg H_2SO_4
Alkaline	0.0001 mol/kg NaOH
inert	0.2 mol/kg buffer solution (equal parts sodium borate/boric acid)
Brine	0.01 mol/kg NaCl
Acidic brine	0.0001 mol/kg H_2SO_4+0.01 mol/kg NaCl
Alkaline brine	0.0001 mol/kg NaOH +0.01 mol/kg NaCl

iii. Depending on whether the solution should be aerated or deaerated, sparge with air or UHP argon. Guidance for sparging times may be found in standard ASTM G2 (150cm^3/min for a minimum of ½ hour) [1].
iv. **Notes:**

1. The pH is not specified in any test, and is let to 'wander'. While not required, it may be prudent to record the pH for all tests so that this information may be referenced in the future.

c. **WE preparation**
   i. Obtain alloy sample.
   ii. Connect a wire to the WE. Test connection using an ohm meter; a reading above 10 ohm is unacceptable.
   iii. Mount specimen in nonconductive epoxy. Ensure electrical connection to WE that will connect to potentiostat is insulated so that only the desired area of the WE contacts solution.
   iv. The final step in surface preparation should be wet polish with 600 grit SiC paper until previous scratches are removed, rinse and dry.
   v. Clean WE ultrasonically, with methanol or ethanol for 5 min. Let dry.
   vi. Calculate or measure exposed WE surface area, and record in notebook: area, accuracy, and method/program used to calculated area.
   vii. Notes:
      1. There are two methods of preparing the working electrode, 1 if the working electrode is from an oxidized alloy sample, and another if the working electrode is from an unoxidized/fresh alloy sample. The above procedure is for an unoxidized sample. One has yet to be written for an oxidized sample.
      2. Whenever convenient, it is recommended to standardize materials. That is, purchased in bulk by one laboratory and dived up, to ensure equivalent alloy formulations. This is especially the case for austenitic stainless steels, which can vary widely in composition. Because of this, NIST standard SRM 160b 316SS should be used initially for AWF tests.

d. **CE preparation**
   i. Ensure CE is clean prior to use.
   ii. Notes:
      1. While not required, a Pt or platinized CE is recommended. Care should be used if using a graphite CE so that impurities are not present that may permeate the graphite and contaminate later tests.

e. **RE preparation**
   i. Ensure that the RE is properly stored prior to use as per manufacturer directions.
   ii. Ensure calibration of RE.
   iii. Record RE type.
   iv. If using a SCE, ensure that the salt bridge is initially saturated in KCl.
   v. Notes:

1. For a SCE, proper storage may involve ensuring the tip is kept in a saturated KCl solution. This can help to avoid KCl crystal formation in the vycor tip region of some types of SCE.
2. It is suggested that the calibration of the measurement cell RE be periodically checked against another RE kept solely for this purpose.

f. **Corrosion cell preparation**
   i. The corrosion cell consists of the solution container, WE, CE, RE, and reference solution.
   ii. Identify and record amount of solution used for testing.
   iii. Polish WE surface just prior to insertion into cell if a fresh surface is desired. Skip this step if an oxidized sample is being used.
   iv. Insert the WE, prepared earlier following the **WE preparation procedure**, into the assembly. Insert CE and RE.
   v. View WE to see if bubbles are stuck to the alloy surface on the WE. If bubbles are present, stir solution or use ultrasonics to remove bubbles.
   vi. Ensure solution temperature is 22 °C ± 3 °C.
   vii. Notes:
      1. If a deaerated solution has come into contact with air briefly during introduction into the cell, an additional sparging period after corrosion cell assembly may be necessary.
      2. For cells operated with possible air exposure, the sparging tube may be pulled out of liquid after liquid transfer, just above the surface, allowing for continued gas flow so as to maintain the gas of interest in and above the solution.

g. **Clean-up Procedure**
   i. Remove and rinse RE with DI water. Store RE per manufacturer's directions. Remove and rinse CE with DI water, place in CE receptacle.
   ii. Remove WE, rinse with DI water, dry, place in storage receptacle.
   iii. Remove and rinse bubbler and place on clean surface or in receptacle suitable for storage.
   iv. If used, remove and rinse pH meter with DI water, place in pH meter receptacle.
   v. Remove and rinse thermometer with DI water, place in storage receptacle.
   vi. Rinse electrode container with DI water.

5. Experimental Procedure

a. Record solution temperature just prior to measurement.

b. **Potentiostat set-up**

Ensure that measurements follow the parameters listed in table 2 if measurements are meant to be compared between laboratories. Record any deviations from those parameters listed in table 2 and the reason form them.

Table 2. Linear polarization resistance measurement.

Parameter	OCP	LPR	CPP	EIS
I Data Points per ΔE	NA	1 pt / mV	1 pt / mV	
E Data Points per Δt	≥0.01 Hz	-	-	
Scan rate, mV/sec	-	0.10	0.1	
Initial Potential, V vs. OC	-	-0.03		
Vertex Potential, V vs. Ref	-	NA		
Final Potential, V vs. OC	-	0.03		
Frequency range used	-	-	-	
Amplitude of Sinusoidal voltage	-	-	-	

c. **Open Circuit Polarization (OCP) procedure.**
   i. Let OCP measurement continue for 4 hours.
   ii. Note if unstable after 4 hours. Stable is considered less than a 20 mV drift over a 5 minute period.

d. **EIS Procedure**

e. **Linear Polarization Resistance (LPR) procedure**

f. **CPP**

6. **Standard Reference plots**

7. **Precision and Bias**

8. **Keywords**

Sample solutions

Table 3 can be used as a guide to formulate solutions for the electrochemical tests that will adhere to the concentration requirements for the solutions listed in table 2.

Table 3. Example solution directions. Note: for example only, it is not needed to follow these directions exactly.

Solution composition	Reagents	Mass of Reagent needed	Alternative procedure
0.0001 mol/kg H_2SO_4	20% (w/w) H_2SO_4 (fisher # 816632)	0.049 g 20% (w/w) H2SO4 1000 g H2O	**Stock Solution** 1.00 g 20 % w/w H2SO4 and 999 g H2O to make stock 0.00204 mol/kg H2SO4 solution **Test solution** add 49.0 g stock to 951 g H2O
0.0001 mol/kg NaOH	3% (w/w) NaOH (fisher # 7245 1)	0.133 g 3% (w/w) NaOH 1000 g H2O	**Stock Solution** 10.0 g 3 % (w/w) NaOH to 990 g H2O to make stock 0.0075 mol/kg NaOH solution **Test solution** add 13.3 g stock to 987 g H2O
0.2 mol/kg buffer solution (1:1 sodium borate:boric acid)	$Na_2B_4O_7 \cdot 10H_2O$ (fisher # MSX03551) H_3BO_3 (fisher # AC31518-5000)	76.3 g $Na_2B_4O_7 \cdot 10H_2O$ 12.4 g H_3BO_3 964 g H2O	-
0.01 mol/kg NaCl	NaCl (fisher # ICN1028925)	0.584 g NaCl 1000 g H2O	
0.0001 mol/kg H_2SO_4+0.01 mol/kg NaCl	20% (w/w) H_2SO_4 (fisher # 816632) NaCl (fisher # ICN1028925)	0.584 g NaCl added to 0.0001mol/kg H2SO4 solution	-
0.0001 mol/kg NaOH +0.01 mol/kg NaCl	3% (w/w) NaOH (fisher # 7245 1) NaCl (fisher # ICN1028925)	0.584 g NaCl added to 0.0001mol/kg NaOH solution	-

3

6

Sample sheet for information to record

Note: this is a guide only. It is recognized that it may not be pertinent or possible to obtain all of the below information. Items listed with an asterisk are items that are deemed of high importance.

Material Identification

Unique material identification label	
Identify QA level	
Formulation	Attached, or location and filename of word/excel file.
Intended use of material	
Production date(s)	
Production location	
Principle investigator	
Radionuclide content (mass %)	
Comments by producer	
Distribution of material to participating labs	

Format: WORD document with tabulated formulation exportable to EXCEL (list filename and location if applicable)

Corrosion Cell Set-Up

Unique material identification label	
Identify QA level	
Reference electrode used	
Counter electrode used	
WE material	
WE surface finish (oxidized, polished to 600 grit…)	
WE surface area	
Non-conductive epoxy used for WE	
Identify and describe test generating sample (if analyzing a reacted specimen)	
Identify calibration of potentiostat (If current, or date of last calibration)	
Identify calibration of thermometer (If current, or date of last calibration)	
Identify calibration of scale(s) used for solution (If current, or date of last calibration)	
Describe solution in which measurement was made (e.g., composition, pH, temperature)	
Estimated uncertainty in measured E and I values as given by potentiostat manufacturer.	
Comments by producer	
Distribution of material to participating labs	

Format: WORD document with tabulated formulation exportable to EXCEL (list filename and location if applicable)

Appendix B

Electrochemical Measurements: Linear Polarization Plots with Stern-Geary, Tafel or Manual fits

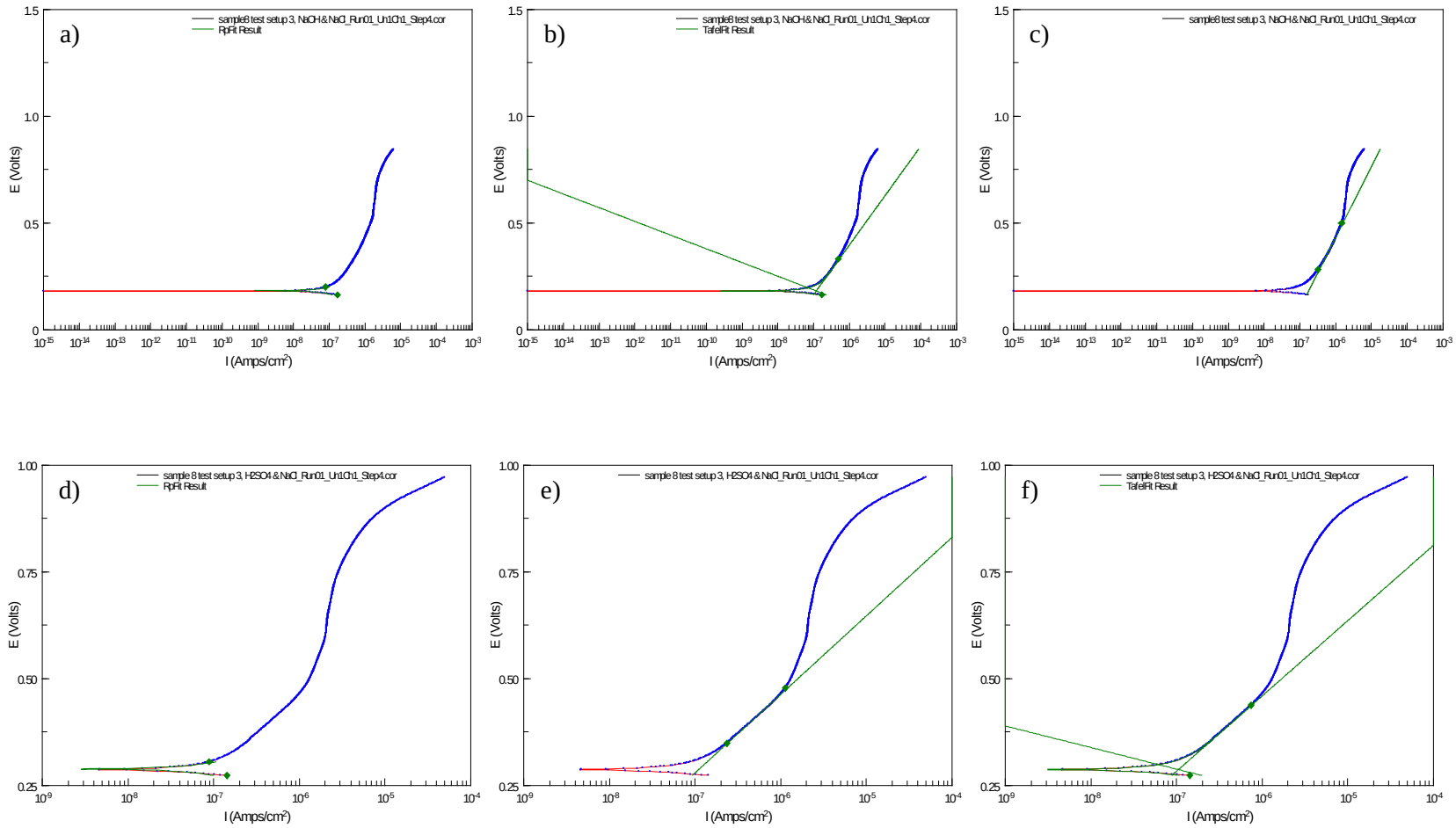

Figure 1-B. Linear polarization measurement of Pellet #8 in basic + brine solution a) Stern-Geary fit, b) Tafel (auto), c) Tafel (manual anodic only), acidic + brine solution d) Stern-Geary fit, e) Tafel (auto), f) Tafel (manual anodic only).

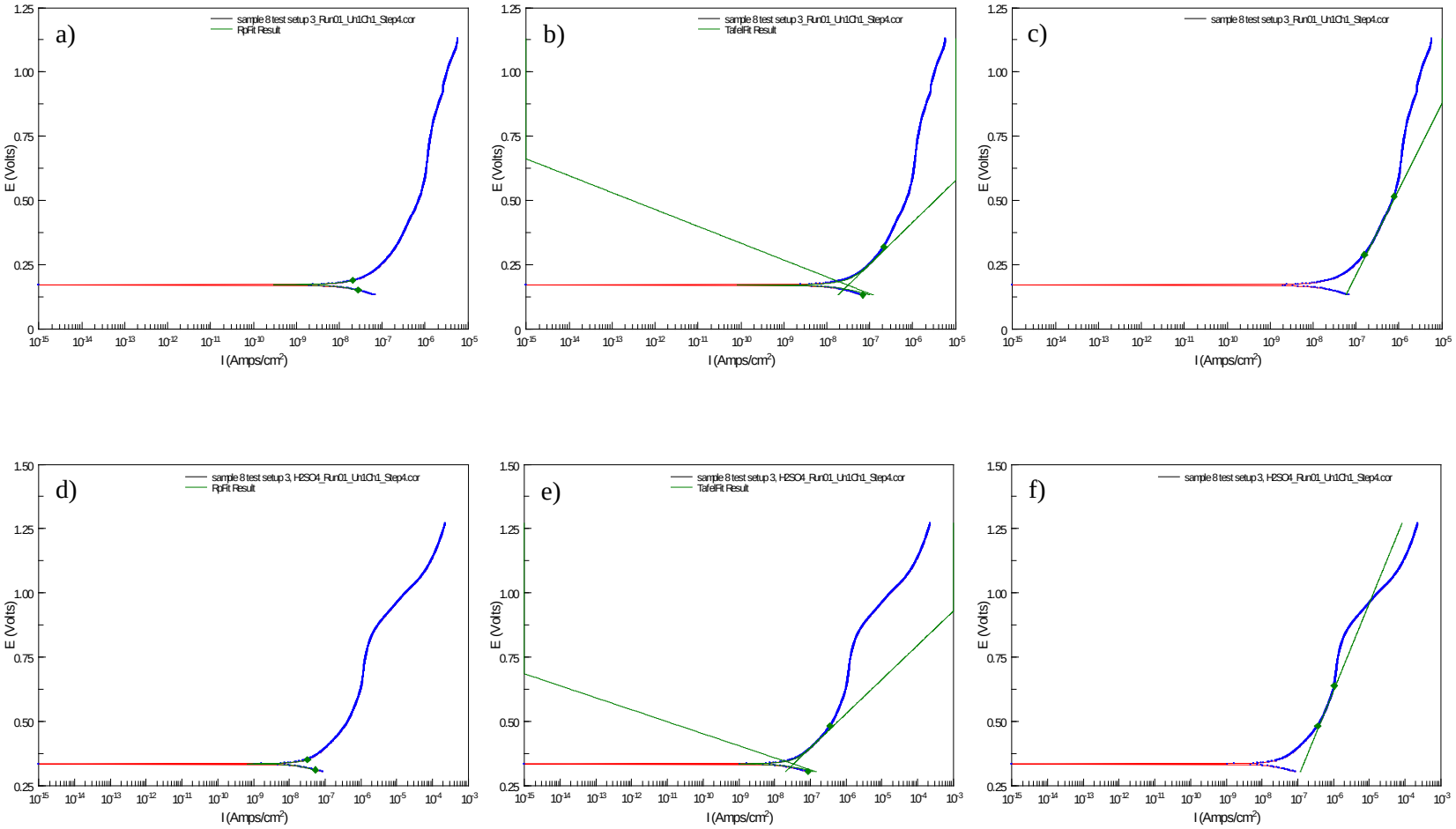

Figure 2-B. Linear polarization measurement of Pellet #8 in basic solution a) Stern-Geary fit, b) Tafel (auto), c) Tafel (manual anodic only), acidic solution d) Stern-Geary fit, e) Tafel (auto), f) Tafel (manual anodic only).

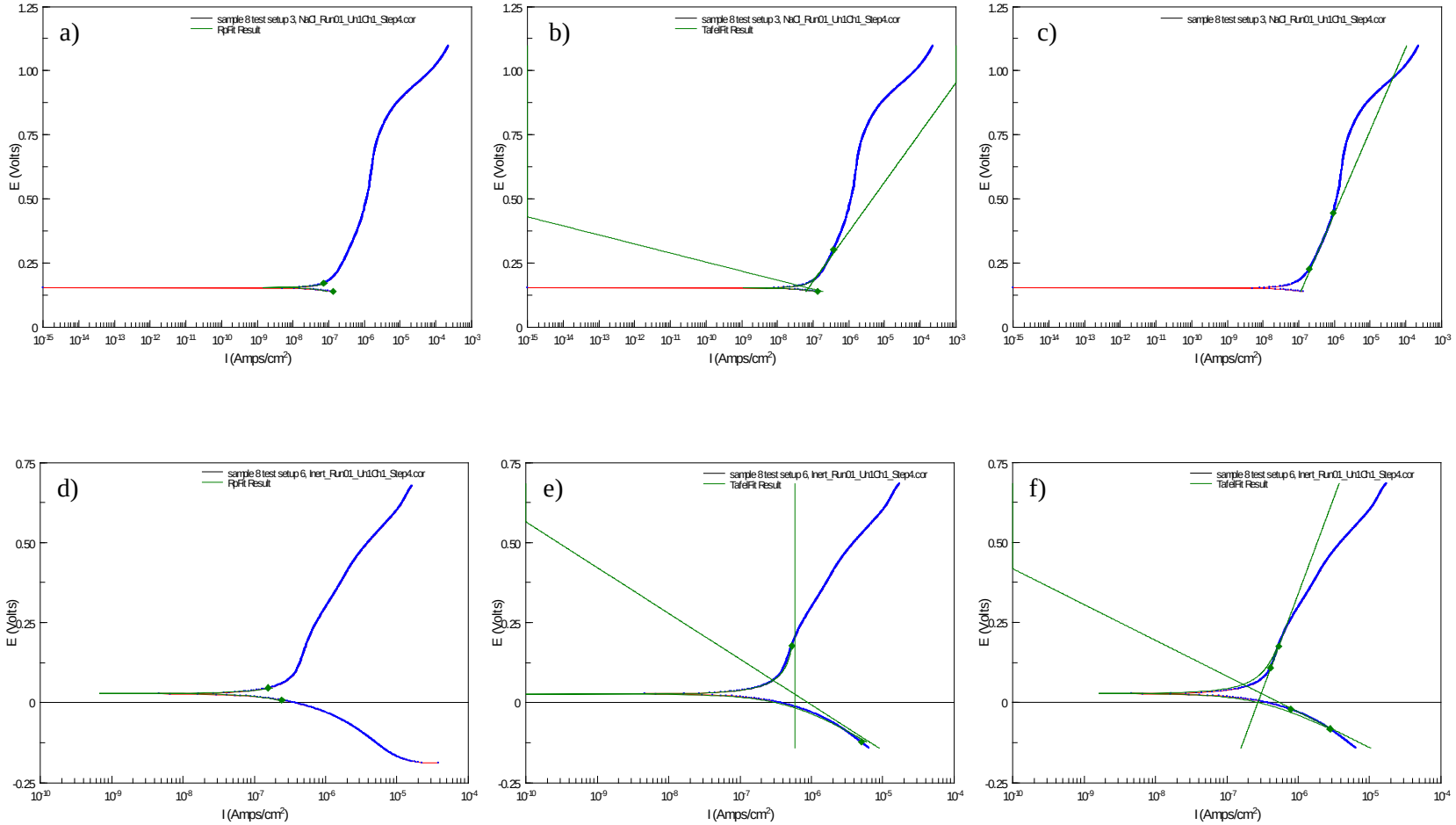

Figure 3-B. Linear polarization measurement of Pellet #8 in brine solution a) Stern-Geary fit, b) Tafel (auto), c) Tafel (manual anodic only), inert solution d) Stern-Geary fit, e) Tafel (auto), f) Tafel (manual anodic only).

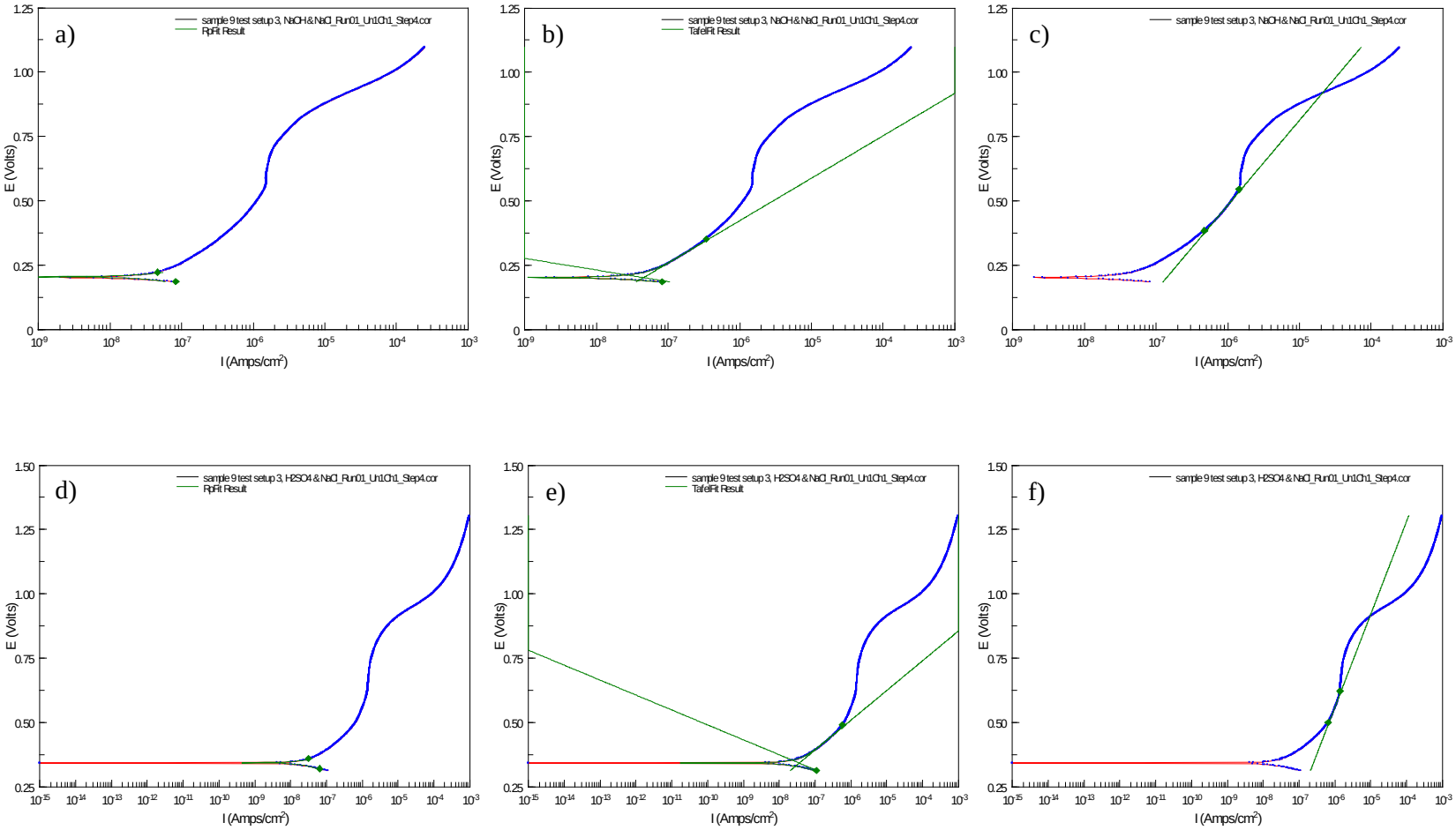

Figure 4-B. Linear polarization measurement of Pellet #9 in basic + brine solution a) Stern-Geary fit, b) Tafel (auto), c) Tafel (manual anodic only), acidic + brine solution d) Stern-Geary fit, e) Tafel (auto), f) Tafel (manual anodic only).

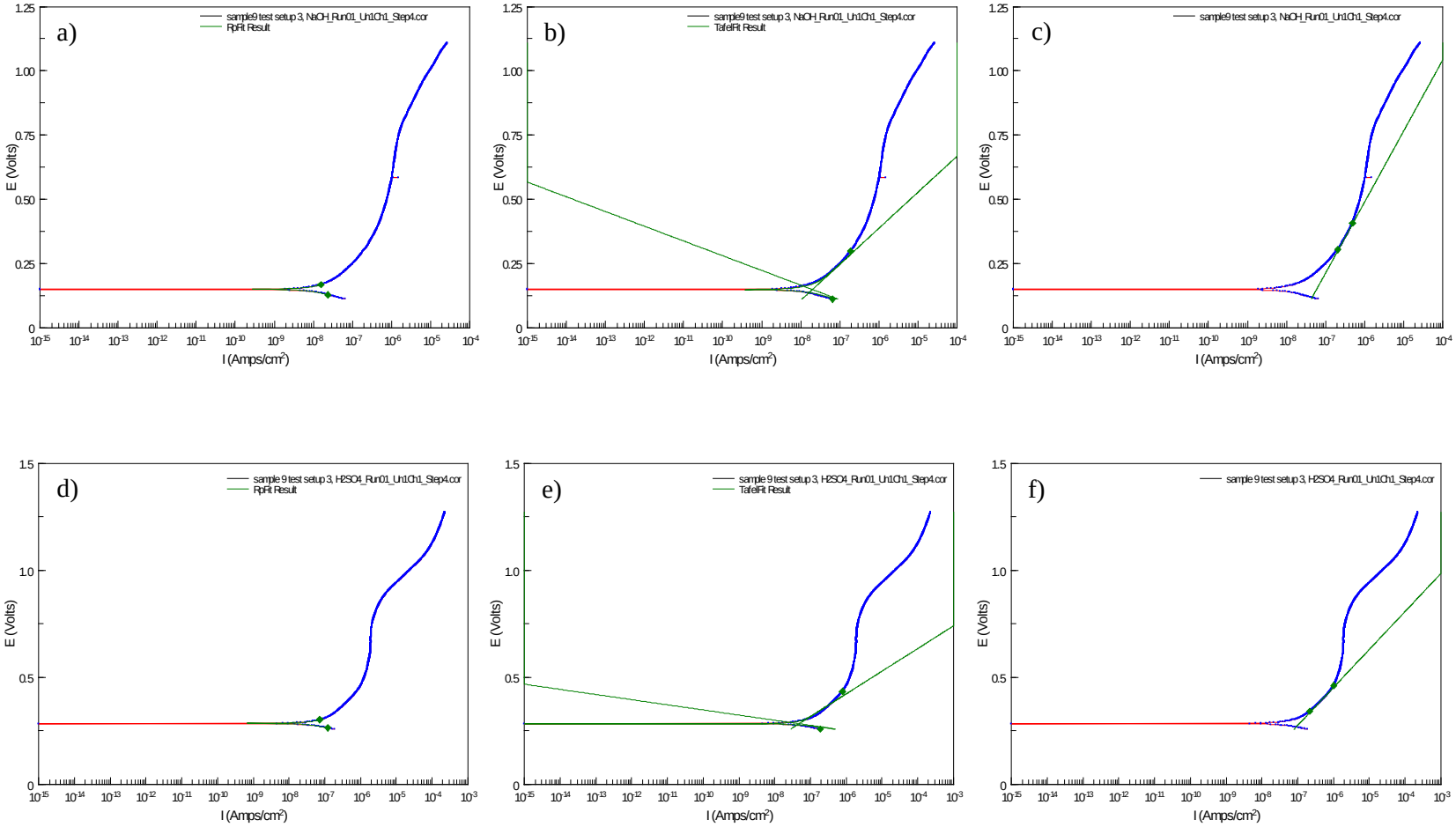

Figure 5-B. Linear polarization measurement of Pellet #9 in basic solution a) Stern-Geary fit, b) Tafel (auto), c) Tafel (manual anodic only), acidic solution d) Stern-Geary fit, e) Tafel (auto), f) Tafel (manual anodic only).

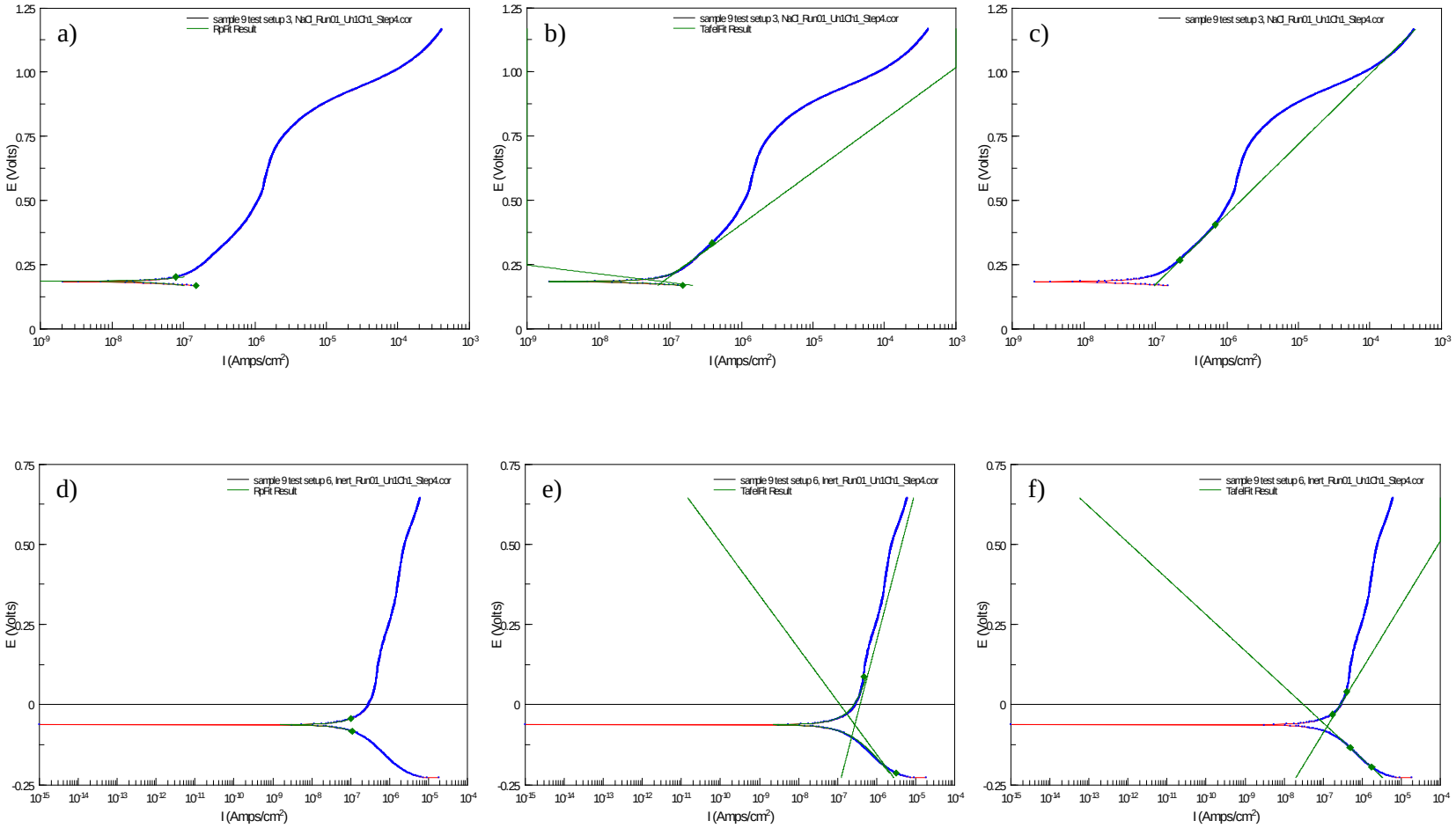

Figure 6-B. Linear polarization measurement of Pellet #9 in brine solution a) Stern-Geary fit, b) Tafel (auto), c) Tafel (manual anodic only), inert solution d) Stern-Geary fit, e) Tafel (auto), f) Tafel (manual anodic only).

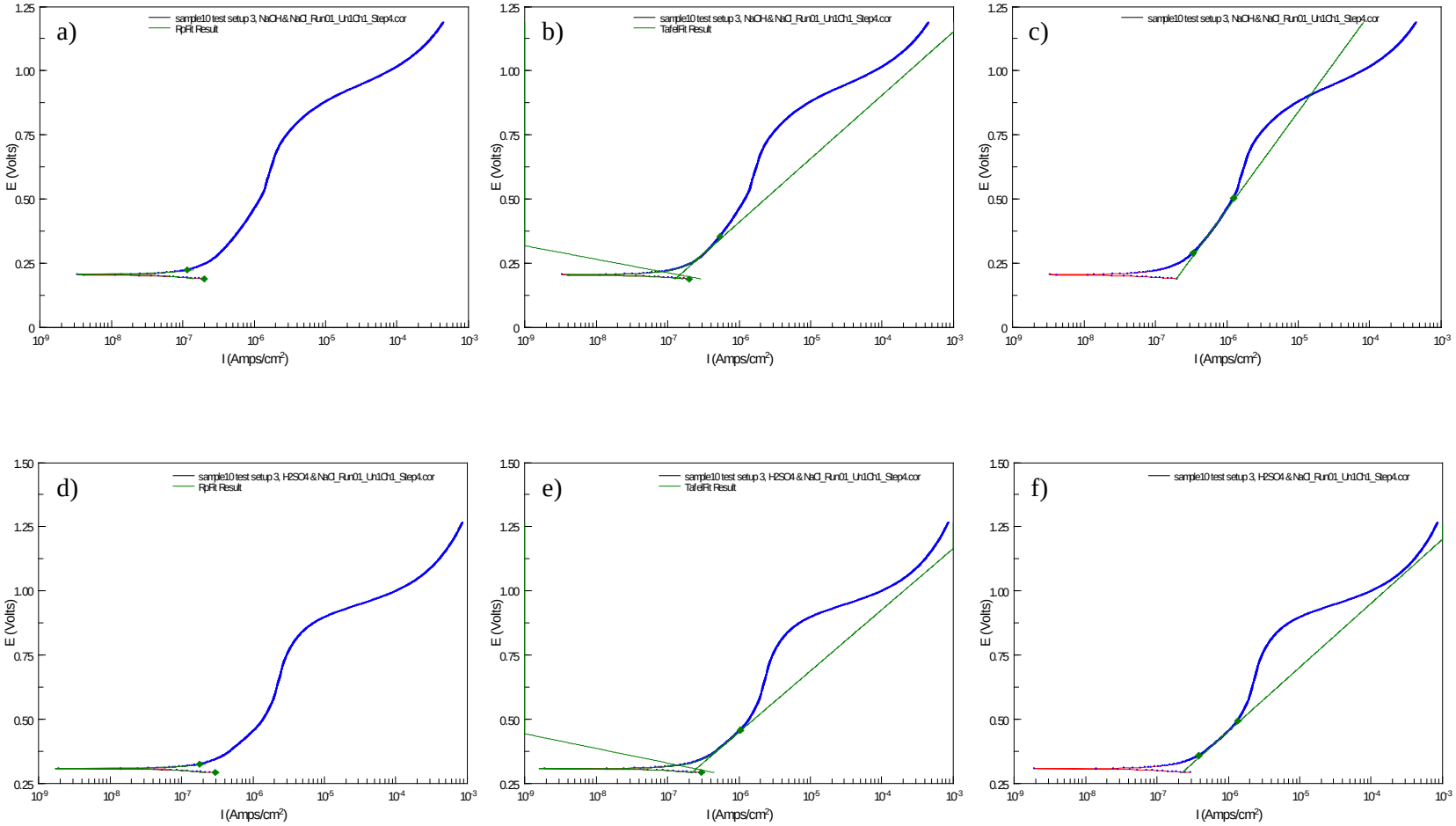

Figure 7-B. Linear polarization measurement of Pellet #10 in basic + brine solution a) Stern-Geary fit, b) Tafel (auto), c) Tafel (manual anodic only), acidic + brine solution d) Stern-Geary fit, e) Tafel (auto), f) Tafel (manual anodic only).

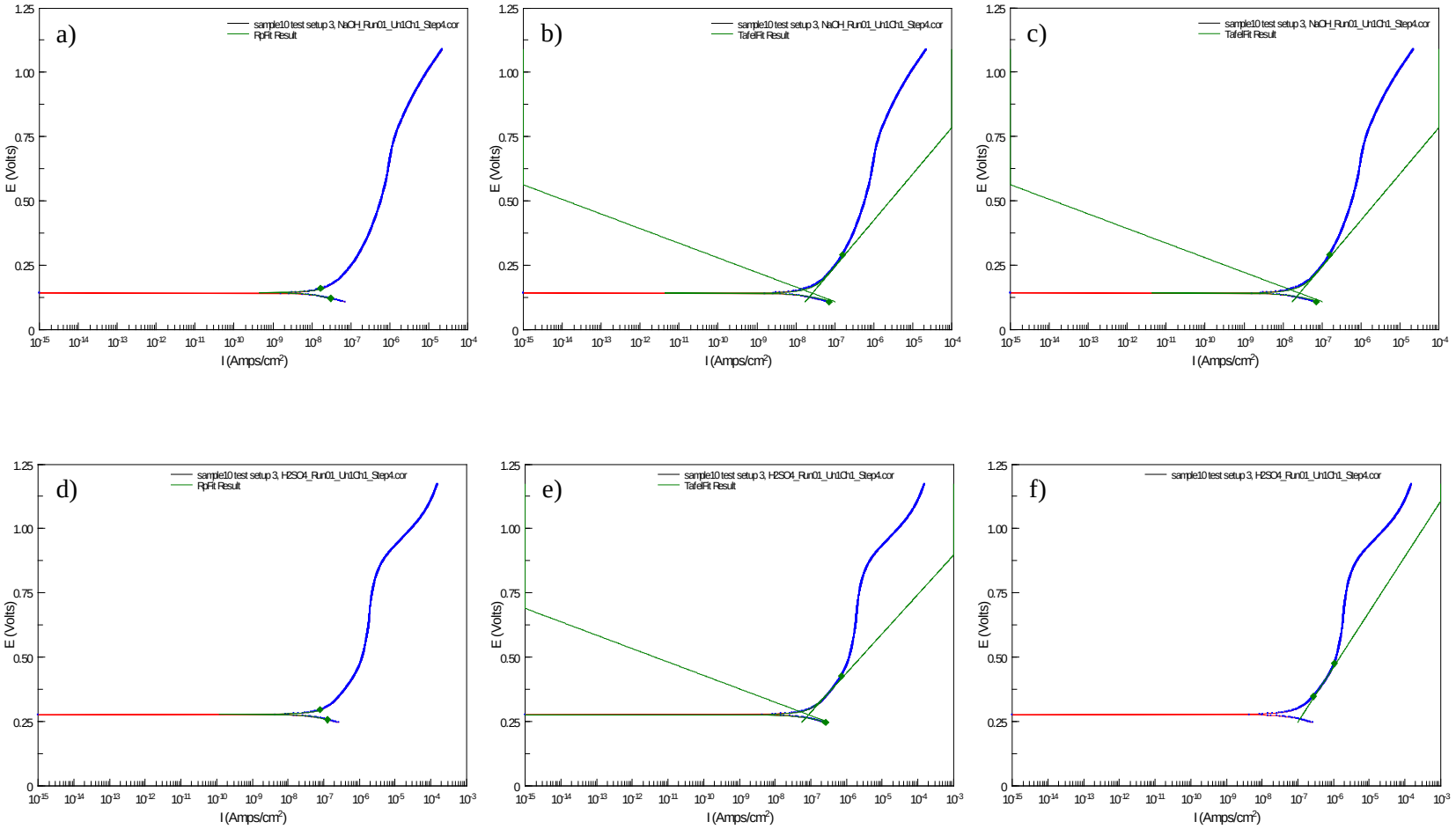

Figure 8-B. Linear polarization measurement of Pellet #10 in basic solution a) Stern-Geary fit, b) Tafel (auto), c) Tafel (manual anodic only), acidic solution d) Stern-Geary fit, e) Tafel (auto), f) Tafel (manual anodic only).

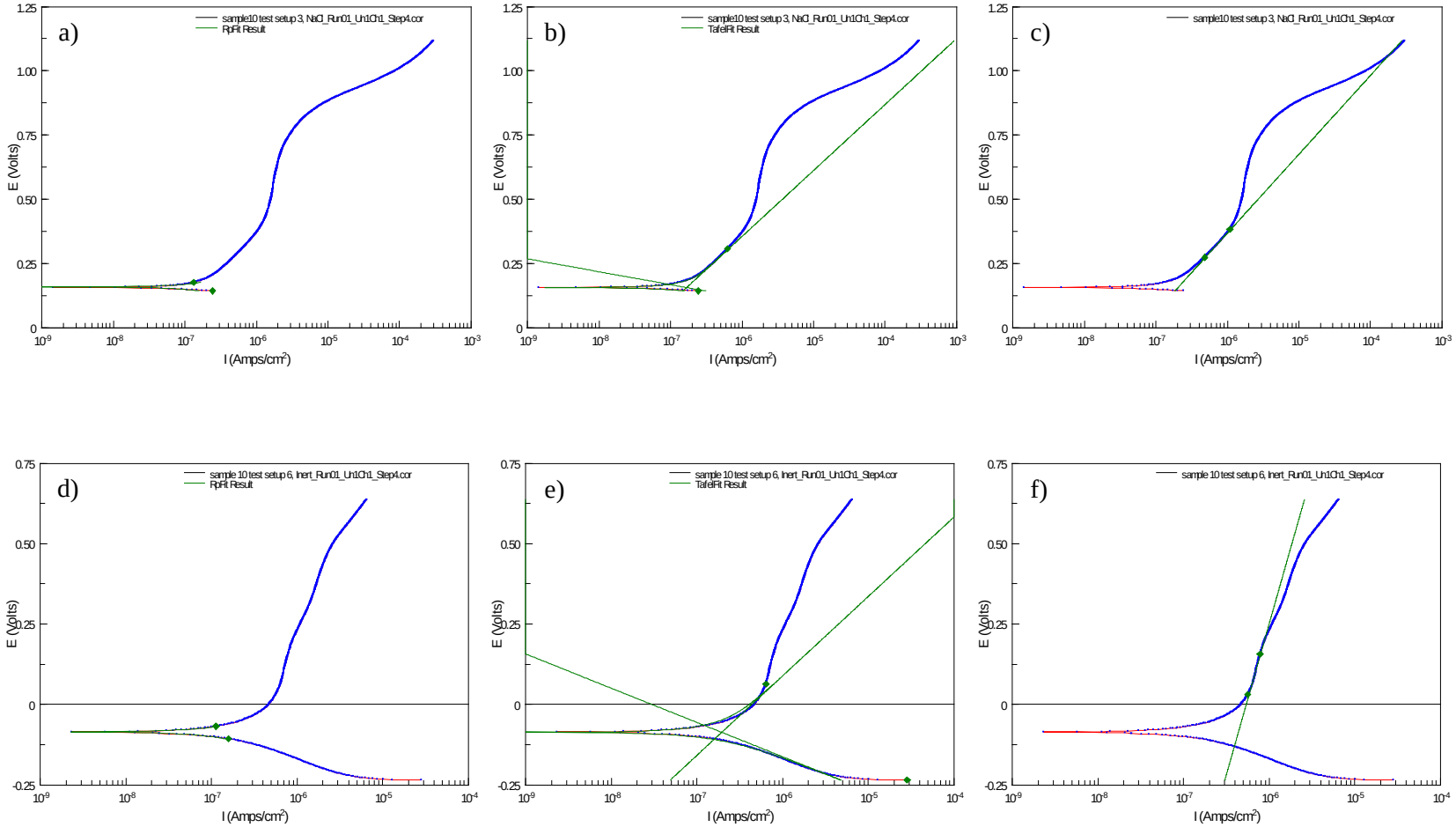

Figure 9-B. Linear polarization measurement of Pellet #10 in brine solution a) Stern-Geary fit, b) Tafel (auto), c) Tafel (manual anodic only), inert solution d) Stern-Geary fit, e) Tafel (auto), f) Tafel (manual anodic only)